Research Article

Cobalt(II) Nanoclusters Incorporated in Ordered Mesoporous Al$_2$O$_3$ for Stable and Coke-Resistant Propane Dehydrogenation

Fabian Ebert, Piyush Ingale, Sarah Vogl, Sebastian Praetz, Christopher Schlesiger, Nils Pfister, Raoul Naumann d'Alnoncourt, Beatriz Roldán Cuenya, Arne Thomas, Esteban Gioria,* and Frank Rosowski

Read Online

ACCESS | Metrics & More | Article Recommendations | SI Supporting Information

ABSTRACT: Due to their availability, low cost, and activity, cobalt-based catalysts are a promising alternative to platinum for the industrial propane dehydrogenation processes. However, their low stability due to sintering, phase transformation, and coke deposition leads to severe deactivation. In this work, the synthesis of amorphous, ordered mesoporous alumina with stabilized Co^{2+} nanoclusters (Co-m-Al$_2$O$_3$) via an evaporation-induced self-assembly synthesis route is presented. The ordered mesoporous alumina is characterized for containing a large amount of defective pentacoordinate Al^{3+} sites and a small amount of strong acid sites. The incorporation of Co^{2+} clusters within the m-Al$_2$O$_3$ structure enhances the dispersion and stability and preserves their reduction even after prolonged time on stream. This leads to a highly selective and steady catalytic performance in the propane dehydrogenation reaction under industrial-relevant conditions. A significantly low deactivation rate of 0.53 d^{-1} with stable propylene selectivity of 95% is observed after 23 h, resulting in a 117% higher space−time yield toward propylene compared to the state-of-the-art impregnated Co/γ-Al$_2$O$_3$ catalyst. Furthermore, Co-m-Al$_2$O$_3$ leads to 4.6 times less coke formation, measured *in situ* for the first time. The detailed study of the nature of the cobalt sites, together with the acidic properties of the alumina supports, provides a deeper understanding of cobalt-based catalysts for dehydrogenation reactions.

KEYWORDS: propane dehydrogenation, cobalt nanoclusters, ordered mesoporous alumina, coke formation, catalyst stability, catalyst regeneration
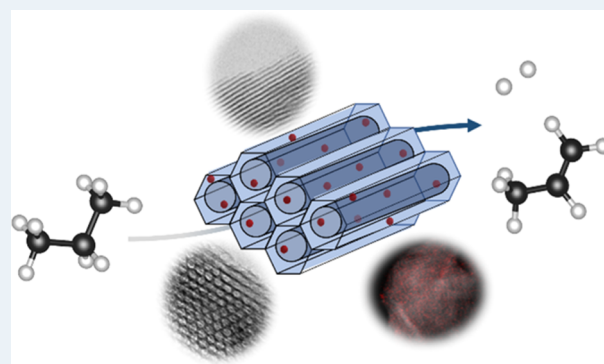
INTRODUCTION

Propylene is an important building block for the chemical industry, as it is an intermediate for many valuable products like acrolein, polypropylene, and acetone.[1−3] Because of its increasing demand, conventional production processes like fluid catalytic cracking and steam cracking are no longer sufficient. Therefore, on-demand propane dehydrogenation (PDH) technologies are required.[4,5]

Industrially applied catalysts either belong to the family of CrO$_x$ or Pt supported materials. The Catofin process employs a chromia/alumina catalyst on parallel adiabatic fixed-bed reactors, which operates at temperatures between 560−650 °C and a reduced pressure of 0.2−0.5 bar.[2,6,7] Due to carbon deposition and deactivation, the operation period of one reactor is limited to 15−25 min. Afterward, the catalyst needs to be regenerated. CrO$_x$ catalysts exhibit a lower space−time yield than Pt catalysts, and the environmental and toxicity aspect of CrO$_x$ disposal make the application less attractive. Platinum-based catalysts, like Pt−Sn−K/Al$_2$O$_3$, show high activity in propane dehydrogenation and are used in industrial processes like the Oleflex technology. A fluidized adiabatic bed reactor together with a regeneration unit is applied in the Oleflex process to enable a continues operation. The reactors are operated at 525−705 °C and 1−3 bar. However, severe deactivation caused by sintering and blockage of the active sites due to coking remain a great challenge.[2,8,9] Furthermore, the scarcity and high price of Pt motivate the development of catalysts based on abundant transition metals.[10]
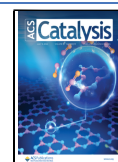
Co-based catalysts have been reported as catalytically active and selective in propane dehydrogenation.[11−13] It is stated that isolated Co^{2+} is the active and selective species for C−H activation, while large agglomeration and reduction to Co^0 promotes C−C bond cleavage and deep dehydrogenation. Therefore, the main challenge in the preparation of a stable,

active, and selective Co catalyst for PDH is the stabilization of Co^{2+} species under harsh reaction conditions.

Increasing the dispersion of the active metal on supports is a common approach in heterogeneous catalysis to enhance the catalytic activity and tune the selectivity for numerous reactions.[14−16] By increasing the dispersion, a large amount of active surface sites is available for the catalytic reaction. Moreover, size-dependent geometric and electronic effects also play a pivotal role.[17,18] Li et al.[19] found that highly dispersed cobalt particles enhance propylene selectivity, while large particles lead to coke formation. This is further emphasized, as the reduction of cobalt oxide is size dependent and large cobalt oxide particles are faster reduced to Co^0.[20]

Moreover, stability is a key factor for a high-performing catalyst. It is highly important to preserve both the oxidation state and the dispersion of the active sites after several hours under harsh reaction conditions. To achieve high stability, a strong interaction between Co^{2+} species and the support through incorporation of the cobalt sites is fundamental for preventing sintering and the formation of large particles. Furthermore, carbon formation on the catalytic surface must be suppressed since it is the main source of deactivation and poor efficiencies in the overall process of propane dehydrogenation.[21]

Herein, a one-pot sol−gel synthesis strategy is applied to highly disperse and stabilize Co^{2+} into an amorphous ordered mesoporous alumina (m-Al_2O_3) of a high surface area. The addition of a Co precursor, together with a structuring agent and an aluminum source, allows incorporation of Co^{2+} nanoclusters within the framework of the ordered mesoporous alumina during its hydrolysis, condensation, and postcalcination process.

To understand the role of different cobalt species in combination with their support, Co was additionally impregnated by state-of-the-art incipient wetness impregnation onto both m-Al_2O_3 and commercial γ-Al_2O_3, resulting in Co sites of different nature and catalytic activities and/or selectivities. γ-Al_2O_3 was chosen as a reference support since it is widely employed for metal−supported catalysts and contains both tetrahedral and octahedral coordinated Al^{3+} sites with a high surface area compared to other Al_2O_3 phases.[22,23] Furthermore, the investigation of the properties and the catalytic behavior of the bare supports, which is often neglected in the literature, was also included. The nature of the active sites together with their respective catalytic performance allows for conclusions on the relationship between the structure and reactivity depending on cobalt as well as support properties.

The stability of the synthesized catalyst was tested under relevant conditions emulating the industrial Oleflex process.[24,25] Although significant studies of Co-based catalysts for propane dehydrogenation have been reported, few have investigated the long-term performance of such catalysts under industrially relevant conditions.[2,26] This work showcases the longest catalytic studies of Co-based catalysts for PDH reported to date, based on long-term 24 h cycles of time on stream followed by regeneration steps.

Coke formation, considered as the most severe cause for fast deactivation in dehydrogenation reactions, was studied both *in situ* and *ex situ*.[21,27] To the best of our knowledge, this is the first *in situ* analysis of carbon deposition rates for cobalt catalysts applied for propane dehydrogenation. Together with Fourier transform infrared (FTIR), thermogravimetric analysis (TGA), laser Raman spectroscopy, and elemental analysis, a deeper understanding of the kinetics of the coking process is presented.

The well-dispersed and stabilized Co^{2+} clusters in the ordered mesoporous alumina, obtained by the one-pot synthesis route, show high activity and remarkable stable selectivity, as well as negligible coke formation. This approach can be envisioned for the rational design of several mono- and multimetallic catalysts. Thus, these findings are of great relevance for the development of active and stable materials applied for thermochemical processes at high temperatures.

■ MATERIALS AND METHODS

Chemicals. All chemicals were used as received without any further purification. Alumina Puralox was obtained from Sasol, Germany. Aluminum isopropoxide (AIP, 98%) and triblock copolymer Pluronic P123 (98%) were purchased from Sigma-Aldrich, Germany. Cobalt nitrate hexahydrate (99%) was purchased from Across Organics, Germany. Nitric acid RotipuranSupra (69%) and anhydrous ethanol (99,5%) were obtained from Carl Roth, Germany. Water HPLC grade was obtained from Honeywell Riedel-de-Haën, Germany.

Synthesis of Ordered Mesoporous Alumina/Cobalt. The catalysts were prepared by the evaporative-induced self-assembly method (EISA). In a typical protocol, 3.6 g of the polymer P123 was dissolved in 80 mL of anhydrous ethanol in a 250 mL round flask, followed by the addition of 6 mL of nitric acid. After vigorous stirring for 30 min, 8 g of aluminum isopropoxide was slowly added. Previously, the aluminum precursor was finely ground to promote the dissolution in the solvent. For the synthesis of cobalt in mesoporous alumina, the desired amount of cobalt nitrate hexahydrate was added directly to the solution prior to the aluminum precursor. The round flask was sealed and vigorously stirred for 5 h. Afterward, a homogeneous white-translucid solution was obtained (pink-translucid for the cobalt-containing solution). The solution was poured into a small beaker (44.2 cm^2 evaporation area) and slowly evaporated and dried for 48 h at 60 °C on static air. The solid product was ground and calcined following a two-step ramp: (a) from room temperature up to 500 °C applying a heating rate of 1 K min^{-1} and a dwell time of 4 h followed by (b) from 500 up to 750 °C employing a heating rate of 5 K min^{-1} and a dwell time of 30 min, under a 500 mL min^{-1} flow of 21% O_2/N_2. The catalysts were named m-Al_2O_3 and Co-m-Al_2O_3, respectively.

Synthesis of the Reference Catalyst. The catalysts were prepared by incipient wetness impregnation. In a typical protocol, 10 g of the commercial Puralox support was impregnated with 5 mL of a cobalt nitrate solution containing the desired amount of the metallic precursor. The nominal metal loading was fixed at 1% wt. The catalyst was dried at 100 °C overnight and calcined at 500 °C for 4 h, applying a heating rate of 10 K min^{-1} and a 500 mL min^{-1} flow of 21% O_2/N_2. The catalyst was named Co/γ-Al_2O_3.

For the sake of studying the influence of the preparation method, a third catalyst was prepared by incipient wetness impregnation of cobalt nitrate hexahydrate on the preformed mesoporous alumina (m-Al_2O_3), followed by thermal treatment at 500 °C for 4 h as described above. The catalyst was named Co/m-Al_2O_3 (IWI).

Characterization. Thermal-gravimetric analysis (TGA) was carried out using an STA 409 apparatus (Linseis) employing 25 mg of the sample at a temperature range of

25−900 °C, with a heating rate of 10 K min^{-1} and a flow rate of 20 mL min^{-1} of 20% O_2/N_2.

Elemental analysis (carbon, nitrogen, hydrogen, and sulfur) was performed on a Thermo FlashEA 1112 organic elemental analyzer by a dynamic flash combustion method operating at 1020 °C. The mean value of three independent experiments is reported.

The morphology, composition, and size distribution of the nanoparticles were analyzed by high-angle annular dark-field-scanning transmission electron microscopy (HAADF-STEM) and energy dispersive X-ray spectroscopy (EDS) elemental mappings in a Thermo Scientific Talos F200X microscope operated at a 200 kV acceleration voltage. The microscope was equipped with a SuperX EDS detector system. Samples were prepared by direct contact with the powder catalysts on lacey carbon 400-mesh gold grids (Plano GmbH). STEM-EDS mappings show the net intensities of the correspondent elements with a postfiltering Gaussian blur of 1.1 sigma.

High-resolution transmission electron microscopy (HRTEM) analysis was conducted using an image cs-corrected "TITAN 80-300 Berlin Holography Special" TEM (FEI/TFS company), operated at 300 kV, equipped with an X-FEG emitter. For image acquisition, an US1000 CCD camera (Gatan Inc.) was used. For determination of the particles lattice plane distances, fast Fourier transform (FFT) of HRTEM images was done using DigitalMicrograph software (Gatan Inc.), and the reflexes were measured manually. Beside HRTEM, also diffraction patterns of larger selected areas (SAED) were acquired and evaluated by measuring the reflexes directly.

The chemical compositions of the catalysts were determined by inductively coupled plasma-atomic emission spectroscopy (ICP-AES) on a Jobin Yvon Horiba - ULTIMA 2000 spectrometer. The calibration standard employed was Trace-CERT 1g/L Co in nitric acid (catalog number: 30329, Merck) for the preparation of calibration solutions. The samples were digested in aqua regia HCl/HNO$_3$ 3:1 v/v (nitric acid 69%, SUPRA-Qualität ROTIPURAN and hydrochloric acid 30%, SUPRA-Qualität ROTIPURAN), and the mean value of three reproducible independent experiments was reported.

Nitrogen sorption analysis was carried out using a Quadrasorb SI (Quantachrome GmbH & Co. KG Odelzhausen, Germany) after degassing the samples for 8 h at 130 °C. The surface area was determined using the multipoint Brunauer−Emmett−Teller (BET) method on the points in the region of $0.05 < P/P_0 < 0.3$, and the corresponding pore size distribution and mean pore size were obtained by applying a Barrett−Joyner−Halender (BJH) model to the desorption values.

X-ray diffractograms were acquired in Bragg−Brentano geometry on a Rigaku SmartLab 3 kW with Cu Kα radiation ($\lambda = 1.54$ Å) over an angular range from 10 to 80° and a scan rate of 2° min^{-1}.

X-ray photoelectron spectroscopy (XPS) was carried out on a Thermo Scientific K-α X-ray Photoelectron Spectrometer. An Al−Kα X-ray source (1486.6 eV) was employed for the analysis, with a pass energy of 200 eV for a survey and 50 eV for high-resolution spectra. The data were collected with an X-ray spot size of 200 µm, 20 scans for a survey, and 50 scans for regions. The analysis of the spectra was done using Avantage software. The C 1s peak of adventitious carbon at 284.8 eV was taken as a reference of charge-shift correction for the measured spectra.

X-ray absorption measurements were carried out with a self-developed wavelength-dispersive spectrometer in von Hámos geometry.[28,29] The spectrometer was equipped with a microfocus X-ray tube, a curved highly annealed pyrolytic graphite mosaic crystal, and a hybrid photon counting CMOS detector with 512 × 1030 pixels and a pixel size of 75 µm × 75 µm. The tube was operated with a voltage of 15.1 kV and a current of 1810 µA. As a reference, a 5 µm Co foil was used. The sample material was pressed as a pellet with a 13 mm diameter by using a hydraulic pellet press with force up to 6 tons for not longer than 60 s. As the samples were measured in transmission mode, the absorption spectrum was acquired by measuring once with and once without the sample. The measurement time for each sample was between 12.5 and 15 h. The samples were measured with two different optics. Both optics are a cylindrically bent highly annealed pyrolytic graphite mosaic crystal with a 5 cm length in the dispersive plane. One optic is optimized for XANES measurements with a crystal thickness of 20 µm and a bending radius of 300 mm to achieve a spectral resolving power of $E/\Delta E = 4000$.[29] The other optic, the so-called multipurpose optic with a crystal thickness of 40 µm and a bending radius of 150 mm, was used to measure the extended X-ray absorption fine structure (EXAFS) region up to 500 eV after the edge with a spectral resolving power of about $E/\Delta E = 2000$.[28] To reduce the absorption of the X-rays in air, vacuum tubes with a Kapton foil as a transmission window have been installed in the beam path. Data normalization was done by X-ray absorption spectroscopy (XAS) analysis and processing software ATHENA, which is part of the Demeter software package.[30] For the EXAFS fitting of the first shell, ARTIMES software of the Demeter package was used.[30] The measurements were performed on the calcined samples with contact with air.

NH$_3$-TPD was measured in an AMI-300 chemisorption analyzer. Fifty milligrams of the dried sample was pulsed 20 times at 90 °C with 40% NH$_3$ in He (50 mL min^{-1}). The saturated sample was subsequently heated to 900 °C with a temperature ramp of 10 K min^{-1} in 40 mL min^{-1} He. The signal was monitored by a linear thermal conductivity detector (TCD). The measured profiles were evaluated by Lorentzian−Gaussian functions fitted by *scipy.optimize.curve_fit*.

FTIR measurements were done in transmission mode on self-supported wafers of an areal density of 20−25 mg·cm^{-2}. Measurements were carried out on a Varian 670 spectrometer equipped with a homemade transmission cell and an MCT detector. The cell was connected to a vacuum system, which achieved a residual pressure of at least 1×10^{-5} mbar and allowed the dosing of gases into the cell. Pyridine was degassed 3 times prior to each measurement. The spectra were recorded with a resolution of 2 cm^{-1} and accumulated 256 scans. An initial spectrum was recorded after dehydration of the sample at 150 °C for 30 min in a dynamic vacuum. The sample was subsequently exposed to 100 mbar H$_2$ and heated to 600 °C with a heating rate of 10 °C·min^{-1}, while the gas atmosphere was exchanged every 15 min after reaching the target temperature. After 1 h at 600 °C, the sample was cooled to 100 °C in a dynamic vacuum. Pyridine was dosed at 100 °C, and a spectrum was recorded after equilibration of 2 min for each dose up to an equilibrium pressure of at least 6 mbar. Weakly adsorbed species were then removed by exposing the sample to a vacuum for 20 min at 100 °C. Difference spectra were calculated by subtracting the absorbance spectrum of the reduced catalyst from the absorbance spectrum of the sample
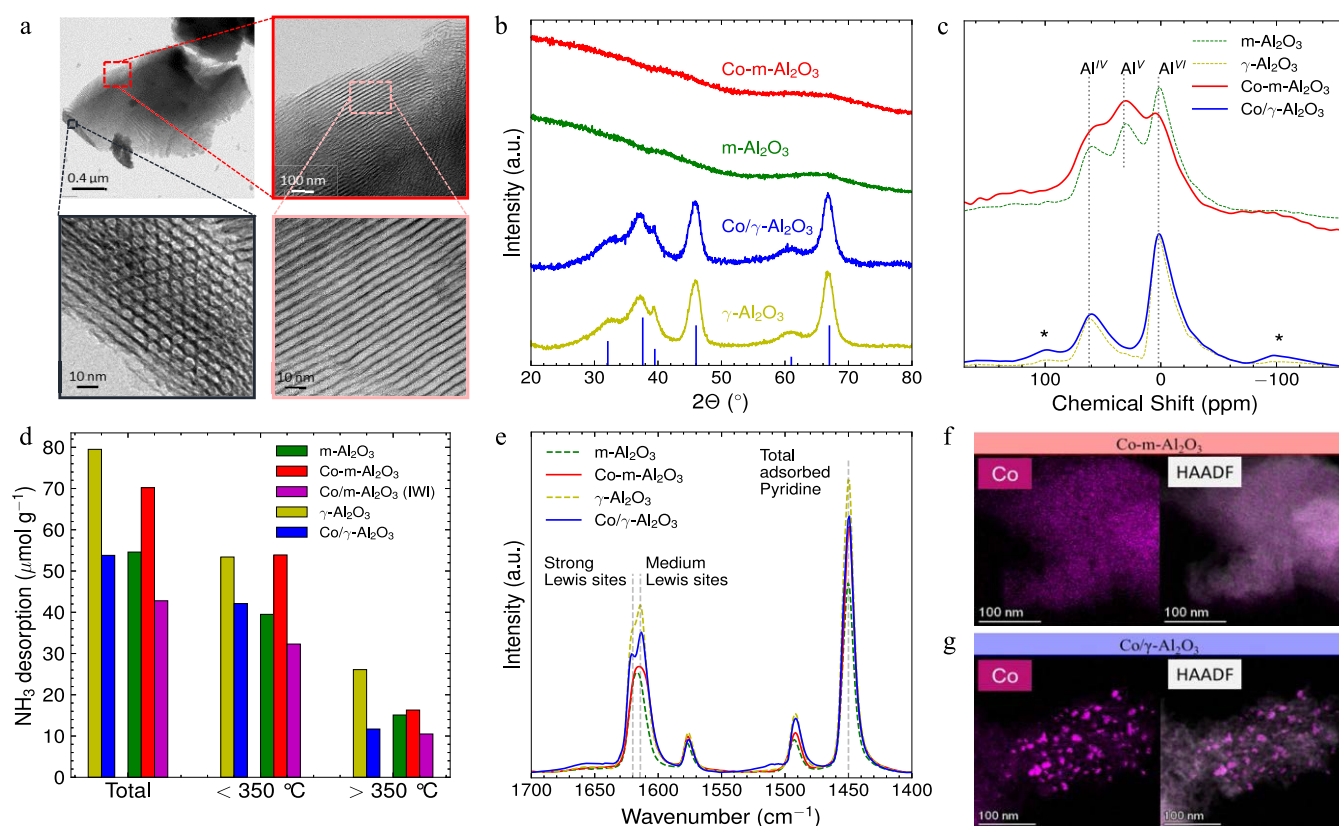
Figure 1. (a) TEM images of Co-m-Al$_2$O$_3$; (b) XRD diffractograms of Co-m-Al$_2$O$_3$, Co/γ-Al$_2$O$_3$, the corresponding alumina supports (m-Al$_2$O$_3$, γ-Al$_2$O$_3$), and γ-Al$_2$O$_3$ reflexes (COD ID: 1531489); (c) ^{27}Al solid-state NMR of cobalt catalysts and bare support (*) spinning side bands; (d) NH$_3$ desorption at different temperatures; (e) pyridine FTIR spectra; and (f, g) HAADF micrographs of STEM analysis together with cobalt mapping by EDS for pristine Co-m-Al$_2$O$_3$ (f) and Co/ γ-Al$_2$O$_3$ (g).

in the presence of pyridine. All presented spectra have been normalized to the areal density of the wafer determined postmeasurement of the mass and dimension of the wafer.

Solid-state diffuse reflectance ultraviolet−visible spectroscopy (UV−vis) spectra have been collected on a Varian Cary 300 UV−vis Spectrophotometer. The spectra were recorded over a wavelength range of 200−800 nm with a data interval of 1 nm. A scan rate of 600 nm/min was employed during data collection. Spectra were obtained using a dedicated cell identified as DRA-CA-301. A white standard of BaSO$_4$ was utilized for calibration purposes. Each spectrum was averaged over a time period of 0.1 s.

Solid-state nuclear magnetic resonance (NMR) measurements were carried out on a Bruker Avance 400 MHz using a 4 mm double resonance spectrometer probe-head operating at a spinning rate of 10 kHz. ^{27}Al-MAS (magic angle spinning) NMR was operated at 104 MHz.

Raman spectra were recorded using the 647 nm emission of a Krypton ion laser (Innova 300c, Coherent) for excitation and a confocal Raman spectrometer (Lab Ram HR- 800 Jobin Yvon) equipped with a liquid-nitrogen cooled charge-coupled device (CCD) camera for data acquisition. The typical laser power at the sample was 1 mW. Spectra were acquired for 5 × 10 s.

The *in situ* coke formation was measured in a Rubotherm magnetic suspension balance (DynTHERM HP-ST, 2010−01001-D). A hundred milligrams of the catalyst was filled in a quartz glass cylinder attached to a quartz glass holder, designed at BasCat and fabricated at TU Berlin. The samples were

heated employing a ramp of 10 K min^{-1} from room temperature up to 600 °C in 50 mL min^{-1} N$_2$. Afterward, the samples were reduced for 1 h in 10% H$_2$ in N$_2$. The gas was then switched to reaction composition (C$_3$H$_8$/H$_2$/N$_2$ = 1:0.5:0.33) at a pressure of 1.1 bar. The weight change was tracked for 24 h. For evaluation of the formed coke, the first measuring point after switching to propane-rich conditions was chosen as a reference point. To consider the buoyancy effect, a measurement without the catalyst was carried out and the weight difference was subtracted from the coking curves.

Catalytic Propane Dehydrogenation. The catalytic experiments were carried out at atmospheric pressure and 600 °C in a modified setup originally designed by Integrated Lab Solutions (Germany). The setup was controlled and the data were collected by hteControl. The collected data were saved and managed by myhte. A quartz tube with an inner diameter of 4 mm was employed as a fixed-bed reactor. Catalyst amounts were fixed to 500 mg for all catalytic tests. In an activation step, the catalysts were first heated to 600 °C with 10 K min^{-1} and reduced *in situ* for 60 min in 50 mL min^{-1} 10% H$_2$/N$_2$. After purging with 50 mL min^{-1} N$_2$ for 5 min, the gas flow was switched to 17 mL min^{-1} of the composition C$_3$H$_8$/H$_2$/N$_2$ = 10:5:2. The resulting w8 hly space velocity (WHSV) was 2.4 g$_{C_3H_8}$ g$_{cat}$$^{-1}$ h^{-1}. The effluent gas stream was analyzed by an online gas chromatograph (Agilent 7890A) equipped with a flame ionization detector and a thermal conductivity detector. Propane conversion, propene selectivity, effective reaction rate, and space−time yield (STY) were calculated according to eqs 1−4, respectively

$$X_{C_3H_8} = \frac{\dot{n}_{C_3H_8,0} - \dot{n}_{C_3H_8}}{\dot{n}_{C_3H_8,0}} \qquad (1)$$

$$S_i = \frac{x_i \dot{n}_i}{\sum_{j \neq C_3H_8}^{N} x_j \dot{n}_j} \qquad (2)$$

$$r_{eff} = \frac{\dot{n}_{C_3H_8,0} X_{C_3H_8}}{m_{cat}} \qquad (3)$$

$$STY = \frac{\dot{n}_{C_3H_8,0} X_{C_3H_8} S_{C_3H_6}}{m_{cat}} \qquad (4)$$

where $\dot{n}_i$ is the molecular flow rate of component i, calculated from the volumetric flow and the inert standard $\dot{n}_i = c_i \frac{\dot{n}_{N_2,0}}{c_{N_2}}$, x_i is the carbon number, and m_{cat} is the mass of the tested catalyst.

Catalysts applied for propane dehydrogenation suffer from deactivation due to a combination of several factors, like sintering of active sites, changes in the oxidation state, and blockage due to carbon deposition. Here, we introduce two constants: $k_{d,r}$ describes the overall activity loss, meanwhile $k_{d,STY}$ considers exclusively the propylene production and represents the deactivation of the selective sites until the catalyst is regenerated. The deactivation constants were determined for the first catalytic cycle before regeneration and are defined by a first-order kinetic deactivation model as follows

$$\frac{d(r_{eff})}{dt} = -k_{d,r} \cdot r_{eff} \qquad (5)$$

$$\frac{d(STY)}{dt} = -k_{d,STY} \cdot STY \qquad (6)$$

These deactivation constants combine all deactivation phenomena mentioned above. Therefore, additional key constants are introduced (eqs 7 and 8), quantifying the deactivation without coke and comparing the activity and propylene production at the beginning and after regeneration, assuming all coke is burned during the regeneration process.

$$K_{d,r} = -\frac{\ln\left(\frac{r_{eff}(t = t_{0,reg.})}{r_{eff}(t = t_0)}\right)}{\Delta t} \qquad (7)$$

$$K_{d,STY} = -\frac{\ln\left(\frac{STY(t = t_{0,reg.})}{STY(t = t_0)}\right)}{\Delta t} \qquad (8)$$

In eqs 7 and 8, t_0 and $t_{0,reg.}$ are the times of the first measuring points after activation, while Δt is the time difference without the regeneration time.

RESULTS AND DISCUSSION

Structure, Acidity, and Textural Properties of the As-Prepared Catalysts. The first steps of the synthesis of the ordered mesoporous alumina involve hydrolysis and condensation of the aluminum precursor in the presence of the pore template, obtaining a hybrid inorganic−organic composite. During the calcination treatment, the organic polymer is removed and an amorphous m-Al$_2$O$_3$ phase is formed. The identification of a suitable calcination temperature was performed by thermogravimetric analysis, as described in Figure S1.

Figure 1a shows TEM micrographs of the Co-m-Al$_2$O$_3$ catalyst prepared via the EISA synthesis route. As can be seen, after the evaporation of the solvent and calcination of the catalyst precursor, a well-defined and ordered structure was obtained. The distinctive hexagonal nanostructure obtained after the removal of the polymeric template leads to well-ordered and aligned mesopores of 5 nm. Additionally, no defined cobalt oxide nanoparticles are observed, suggesting a high degree of dispersion on the mesoporous structure. Figure S2 shows the TEM micrographs corresponding to bare m-Al$_2$O$_3$ without the addition of cobalt, showing similar results. Thus, the incorporation of cobalt during the synthetic procedure did not affect the ordered mesoporous structure of the catalyst. Figure S3 shows the respective TEM for Co/γ-Al$_2$O$_3$ prepared by impregnation of the metal precursor on the commercial Puralox, displaying the typical disordered structure of the alumina. The cobalt loading for both catalysts has been verified by ICP-OES (w_{Co}(Co-m-Al$_2$O$_3$) = 1.0 wt %, w_{Co}(Co/γ-Al$_2$O$_3$) = 1.1 wt %).

Also, the ordered structure of Co/m-Al$_2$O$_3$ (IWI) collapses during the impregnation process, as visible in the TEM images of the impregnated catalyst (Figure S4).

The crystalline phases of the calcined materials were characterized by powder X-ray diffraction. As shown in Figure 1b, the addition of cobalt does not change the crystallinity of the catalysts. Both γ-Al$_2$O$_3$ and Co/γ-Al$_2$O$_3$ present a broad peak at 37.5°, together with the peaks at 46 and 67°, which are characteristic of the spinel-type phase of γ-alumina.[31] Aside from the characteristic γ-Al$_2$O$_3$ peaks, no additional diffraction pattern can be observed, indicating that cobalt particles are amorphous or highly dispersed onto the support and/or below the detection limit of the diffractometer.

The m-Al$_2$O$_3$ catalyst prepared by the EISA route shows an amorphous structure in the wide-angle X-ray diffraction (XRD). Meanwhile, the small-angle X-ray diffraction (Figure S5) shows the characteristic (100) diffraction peak of the ordered hexagonal mesoporous structure at around 2Θ 1.0° attributed to the $P6mm$ space group, in agreement with the TEM observations.[32] Moreover, the addition of cobalt during the one-pot synthesis does not affect the amorphous nature of the support (Figure 1b). Similar to Co/γ-Al$_2$O$_3$, there is no evidence of large crystalline cobalt species, indicating that the particles are amorphous and/or well dispersed on the alumina.

Table 1 shows the specific surface area, pore volume, and mean pore size of the cobalt-containing catalysts and the supports. For m-Al$_2$O$_3$, a high surface area of 268 m^2 g^{-1} is obtained. The specific surface areas for Co-m-Al$_2$O$_3$ showed a similar value. Thus, the addition of cobalt during the synthetic

Table 1. Textural Properties Determined by Nitrogen Sorption[a]

sample	BET area (m^2 g^{-1})	pore volume (cm^3 g^{-1})	mean pore size (nm)
m-Al$_2$O$_3$	268	0.47	4.9
Co-m-Al$_2$O$_3$	265	0.49	4.9
γ-Al$_2$or$_3$	189	0.45	6.6
Co/γ-Al$_2$O$_3$	174	0.42	6.6

[a]Surface area was determined by applying the multipoint BET equation, and mean pore size values were obtained from the BJH method.
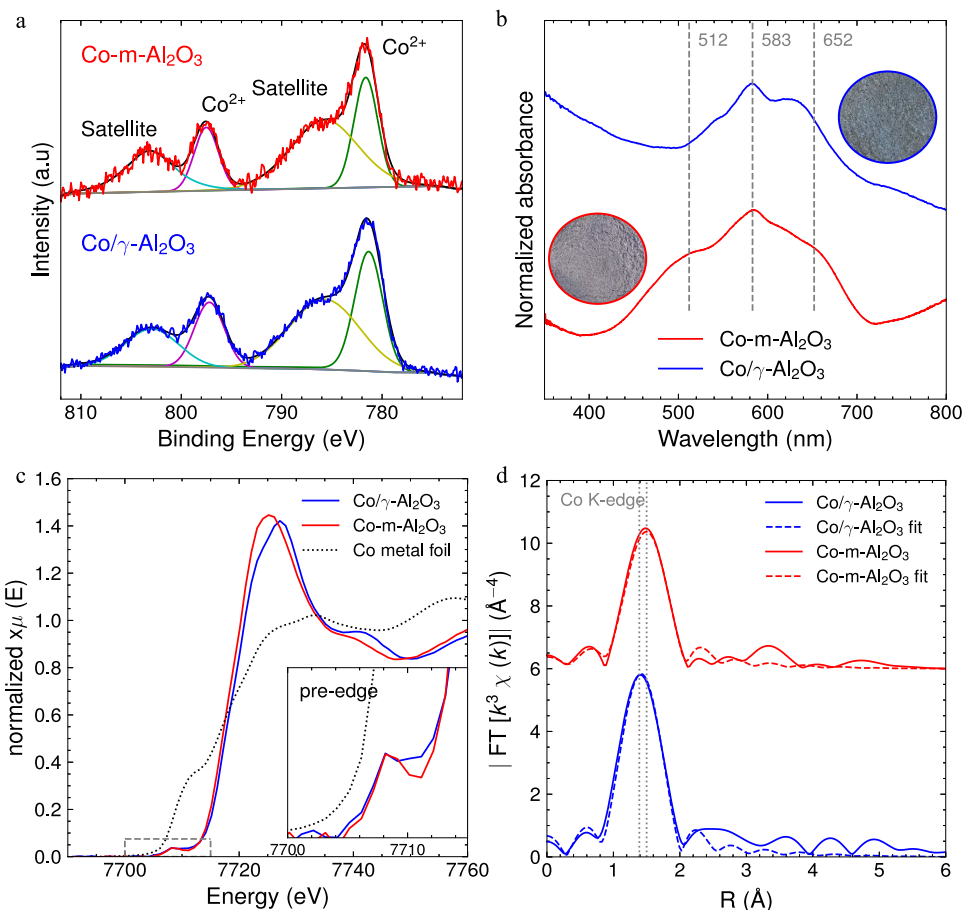
Figure 2. (a) XPS of Co 2p for Co-m-Al$_2$O$_3$ and Co/γ-Al$_2$O$_3$; (b) UV−vis spectra of Co-m-Al$_2$O$_3$ and Co/γ-Al$_2$O$_3$; and (c, d) Co K-edge XANES and Fourier transform (FT) magnitude EXAFS spectra of Co-m-Al$_2$O$_3$ and Co/γ-Al$_2$O$_3$.

route does not affect the textural properties of the material after the calcination step. The mean pore size obtained by the BJH method gives rise to a mean value of 5 nm, in agreement with the ordered mesoporous structured observed by TEM, as shown in Figure 1a. On the other hand, the reference γ-Al$_2$O$_3$ and Co/γ-Al$_2$O$_3$ catalysts show a lower surface area of 189 and 174 m^2 g^{-1}, respectively. Nitrogen sorption isotherms and the pore width distribution for all of the catalysts are given in Figure S6. The Co-m-Al$_2$O$_3$ and m-Al$_2$O$_3$ catalysts have a narrower distribution, with smaller average pore sizes, in agreement with the highly ordered structure of the alumina. Therefore, it is expected that the higher surface area of m-Al$_2$O$_3$ can promote the dispersion of the metal precursor onto the support, together with differences in the nature of the metal oxide−support interaction discussed below.

Solid-state NMR spectroscopy was employed to give more insights into the nature of the different supports (Figure 1c). The contributions of the Al^{3+} sites and their changes after impregnation are shown in Figure S7 and Table S1. Both γ-Al$_2$O$_3$ and Co/γ-Al$_2$O$_3$ do not suffer changes, showing contributions of 70 and 30% in Al$_{octa}^{3+}$ and Al$_{tetra}^{3+}$, respectively. However, Co incorporation onto Co-m-Al$_2$O$_3$ leads to a clear structural change. The content of Al$_{penta}^{3+}$ sites increases from 24 to 54%, and that of Al$_{octa}^{3+}$ sites decreases from 47 to 29%. Al$_{tetra}^{3+}$ sites remained unchanged, with a mean value of 23%.

Within the past decade, the role of unsaturated Al$_{penta}^{3+}$ species as anchoring sites for clusters like Pt, Ru, or Pd was

reported.[33−37] In all cases, Al-NMR studies showed an increase of Al$_{octa}^{3+}$ sites with a respective reduction of Al$_{penta}^{3+}$ sites,[34,35] thus suggesting that metal clusters were anchored on the defective sites. Interestingly, this trend does not agree with our experimental evidence. However, it should be noted that the incorporation of the metallic species on the reported catalysts was based on wet impregnations onto the preformed m-Al2O3 support. Meanwhile, in this work, Co is incorporated in a one-pot procedure following a solgel route.

In agreement with our findings, Li et al.,[38] Yu et al.,[39] and Pan et al.[40] reported that the incorporation of Cr, Zr, and Co species onto ordered mesoporous Al$_2$O$_3$ was followed by an increase of Al$_{penta}^{3+}$ and a decrease of Al$_{octa}^{3+}$ sites. This was attributed to the cross-linkage of the metal and aluminum hydroxyl species during the hydrolysis and condensation steps. Introduction of Co−OH species could promote the dispersion of Al−OH oligomers and prevent their condensation, reducing the formation of alumina clusters of octahedral coordination and promoting an Al−O−Co bond within the mesoporous structure.[41] Thus, Co^{2+} sites were incorporated within the m-Al$_2$O$_3$ framework during the synthesis instead of being anchored to Al$_{penta}^{3+}$ defective sites. This was later verified by means of different spectroscopic techniques and electron microscopy.

It is known that reaction pathways of the propane dehydrogenation, like cracking, hydrogenolysis, and activation of C−H bonds, can take place on Lewis and/or Brønsted acid sites of the support.[42−44] Therefore, the surface acidity of the

catalysts was studied by NH_3-TPD experiments, which indicates the total acidity due to both Lewis and Brønsted sites (Figure 1d). The evaluation of the desorption experiments is described in the Supporting Information (Figures S8, S9 and Table S2), where the desorption area below 350 °C is ascribed to weak acid sites and above 350 °C to strong acid sites.[23,45−49] γ-Al_2O_3 has a larger overall acidity than m-Al_2O_3, especially regarding strong acid sites above 350 °C. The total acidity is reduced when both γ-Al_2O_3 and m-Al_2O_3 supports are impregnated with Co. This suggests that after calcination, cobalt oxide is attached to the surface acid sites, blocking them for NH_3 adsorption. On the other hand, when Co is added through the sol−gel route, the amount of NH_3 desorbed below and above 350 °C was increased. Thus, Co does not block the acid sites on the surface, and together with the results from ^{27}Al solid-state NMR, it can be concluded that cobalt is incorporated in the m-Al_2O_3 structure.

For a more detailed investigation, pyridine IR spectroscopy was also conducted (Figure 1e). The spectral region for the pyridine ring vibration reveals the presence of medium-strong and strong Lewis acid sites for all samples, as indicated by the vibrations between 1650 and 1590 and 1455 and 1441 cm^{-1}.[50,51] A higher total acidity is observed for the two γ-Al_2O_3 based materials, in agreement with NH_3-TPD results. Introducing Co to the system decreases the acidity for Co/γ-Al_2O_3 and increases for Co/m-Al_2O_3. The incorporation of Co into the alumina framework via the one-pot synthesis, hence, causes a redistribution of the acid sites, while impregnation only leads to a blockage of the Lewis acid sites, maintaining the ratio of strong to medium-strong Lewis acid sites. As the Lewis acidity in Al_2O_3-based materials is strongly connected to the presence of undercoordinated Al_{penta}^{3+} sites, the pyridine adsorption confirms the results obtained by ^{27}Al solid-state NMR.[52] None of the samples shows vibrations indicative of strong Brønsted acid sites (PyH^+) at around 1490 cm^{-1}. However, both γ-Al_2O_3 and m-Al_2O_3 possess −OH groups accessible for hydrogen bonding with the pyridine molecule characteristic for weak Brønsted acidity (1608−1590 cm^{-1}).[51]

The cobalt dispersion was investigated by STEM-EDS. Figure 1e clearly shows the high degree of dispersion in Co-m-Al_2O_3, homogeneously distributed over the support. Moreover, higher magnifications revealed very small and well-distributed clusters below 1 nm (Figure S10). The impregnated catalyst, on the other hand, possesses significantly larger agglomerates with an average size of 9.5 ± 3.5 nm (Figures 1f and S11). Crystallites of this size should be detectable in XRD, thus it is inferred that large agglomerates of amorphous cobalt are present.[53] Similarly, the impregnation of m-Al_2O_3 gives rise to an inhomogeneous cobalt dispersion (Figure S12).

XPS analysis of the calcined (21 vol % O_2) Co/γ-Al_2O_3 and Co-m-Al_2O_3 is given in Figure 2a. The ex $situ$ XPS spectra show two main peaks at 781.8 and 797.5 eV, assigned to the Co^{2+} $2p_{3/2}$ and $2p_{1/2}$ spin orbitals, respectively. The strong contributions of the satellite features are characteristics of the O 2p to Co 3d charge transfer effect of paramagnetic Co^{2+} species.[54] As expected, no Co^0 is present at the surface of the calcined sample. These results suggest that the cobalt on the surface of the two catalysts is mainly present as Co^{2+} after calcination and no Co_3O_4 is formed.[55] The catalysts were also activated at 600 °C under 10 vol % H_2 in N_2 for 1 h and inert transferred for XPS measurement to investigate the oxidation state of the cobalt at the beginning of the reaction. For both catalysts, the XPS signal is identical to the calcined samples

(Figure S13), showing that the cobalt is not reduced during the activation procedure and is still present as Co^{2+}. The oxidation state of the calcined catalysts was further confirmed by UV−vis analysis (Figure 2b). An absorption band with three peak maxima at approximately 540, 583, and 630 nm can be identified for Co/γ-Al_2O_3, in agreement to its bluish color. Meanwhile, Co-m-Al_2O_3 shows three characteristic bands centered at 512, 583, and 652 nm. These peaks are assigned to the $[^4A_2(F) \rightarrow {}^4T_1(P)]$ d−d transition of the tetrahedral Co^{2+}.[56−58] The shift toward smaller and higher wavelengths of the two side peaks at 512 and 652 nm was also reported by Pan et al.[40] for ordered mesoporous alumina. These shifts lead to a slightly more purple color and are related to the incorporation of the cobalt species within the alumina framework.[59] In the case of Co_3O_4 formation, two broader bands in the range of 350−450 and 640−730 nm would be expected, ascribed to $[^1A_{1g} \rightarrow {}^1T_{2g}]$ and $[^1A_{1g} \rightarrow {}^1T_{1g}]$ transitions of octahedral Co^{3+}, respectively.[60−62] Therefore, no Co_3O_4 phase and no octahedral Co^{3+} are present in both catalysts.

The coordination and species of the cobalt sites were further investigated by ex $situ$ X-ray absorption spectroscopy. Figure 2c shows the XANES spectra of the calcined Co/γ-Al_2O_3 and Co-m-Al_2O_3 catalysts with the characteristic pre-edge peak at ∼7709.9 eV caused by the 1s → 3d transition.[63] This peak can be found for CoO, $CoAl_2O_4$, and Co_3O_4 structures. However, the edge peak maximum at ∼7725 eV clearly indicates the presence of Co^{2+}; as for Co_3O_4, the peak would shift to higher energies, and an additional shoulder would be seen at lower energies.[64−66] Also, the spectra do not indicate the presence of cobalt in a defined $CoAl_2O_4$ spinel structure. In a comparative study on different cobalt oxide phases by Maurizio et al.,[65] two additional shoulders before the edge peak maximum have been observed for the $CoAl_2O_4$ phase. Despite the fact that the spectra at the Co K-edge are very similar for both samples, a distinct shoulder at ∼7740 eV is observed for Co/γ-Al_2O_3. This is characteristic of larger CoO clusters, in agreement with STEM-EDS results.[67] Figure 2d shows the Fourier transform magnitude EXAFS spectra and fitting results, with a strong peak close to R = 1.5 Å for the first shell Co−O coordination. As can be seen, the average bonding distance of Co−O for Co-m-Al_2O_3 is slightly increased as compared to Co/γ-Al_2O_3. The fit to the first shell returns an increase in the bonding distance of 0.07 Å for the Co−O bond. This agrees with Dai et al.,[12] where a Co−O distance increase of 0.06 Å was observed for cobalt incorporated in mesoporous alumina.

In summary, amorphous alumina with highly ordered mesopores and a surface area than commercial γ-Al_2O_3 is obtained via the EISA synthesis route. m-Al_2O_3 is constituted by tetrahedral, pentahedral, and octahedral coordinated alumina atoms and has a smaller density of acid sites on the surface. Cobalt is present as Co^{2+} in tetrahedral coordination on both calcined catalysts. However, Co^{2+} is highly dispersed and incorporated within the structure in the ordered mesoporous alumina on Co-m-Al_2O_3, while larger agglomerates can be found on the impregnated catalysts.

Catalytic Performance in Propane Dehydrogenation. In the literature, the catalytic performance is often measured under milder conditions, and therefore, higher stability or higher conversions are achieved.[11,68,69] In this work, the stability and selectivity were studied under industrially relevant conditions emulating the industrial Oleflex process, with undiluted propane and a H_2 feed ratio of 2:1.[24,25,70,71]
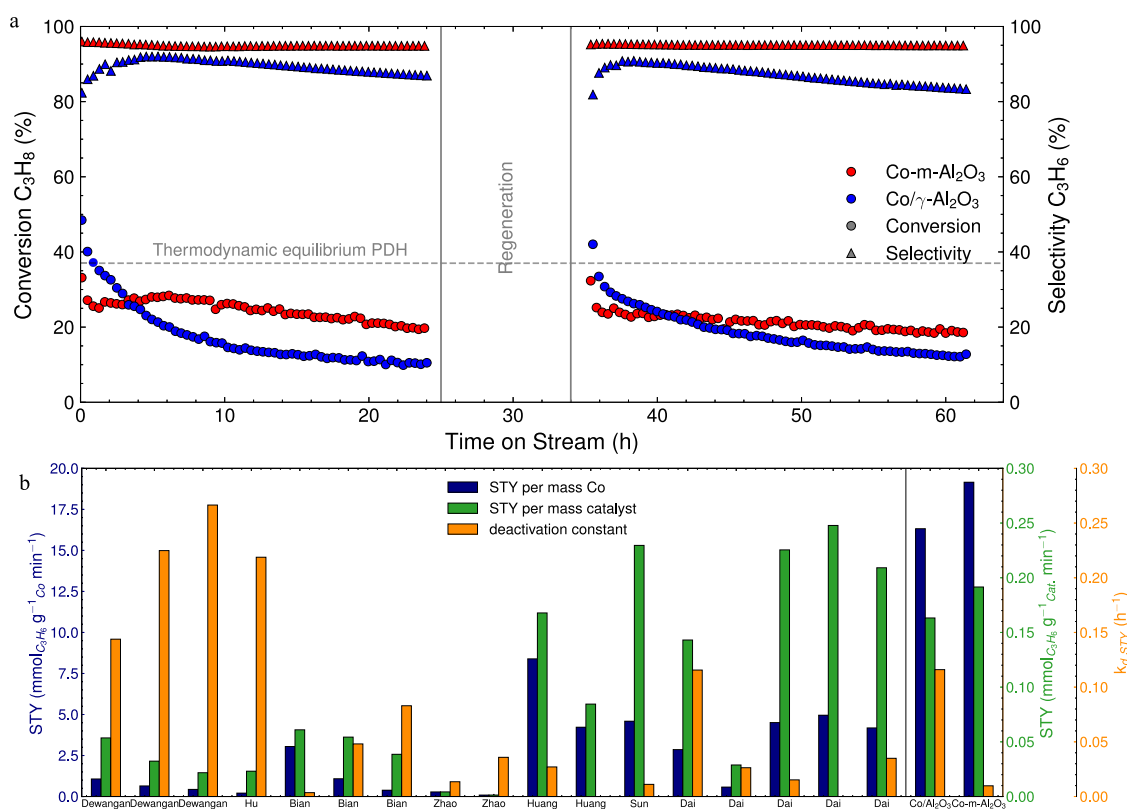
Figure 3. (a) PDH performance with the regeneration cycle after 24 h at 500 °C with 5 and 20% O_2 in N_2 (2 × 1 h). Test conditions: 0.5 g of the catalyst, $C_3H_8/H_2/N_2$ = 10:5:2, WHSV = 2.4 h^{-1}, and T = 600 °C. (b) Space−time yield per mass of cobalt (blue bars) and the mass of the catalyst (green bars) after 5 h of the catalytic test and the deactivation constant (orange bars) calculated between the 1st and the 5th h of time on stream for cobalt catalysts reported in the literature and the catalysts synthesized in this work.

Table 2. Space−Time Yield and the Effective Reaction Rate after 1, 5, and 23 h Catalytic Testing with Corresponding Deactivation Constants Calculated by the First-Order Kinetic Deactivation Model

catalyst	STY (t = 1/5/23 h) ($\mu mol_{C_3H_6}$ g_{cat}^{-1} s^{-1})	r_{eff} (t = 1/5/23 h) ($\mu mol_{C_3H_8}$ g_{cat}^{-1} s^{-1})	$k_{d,STY}$ (d^{-1})	$k_{d,r}$ (d^{-1})	$K_{d,r}$ (d^{-1})
Co/γ-Al_2O_3	4.3:2.7:1.2	5.0:3.0:1.3	2.28	2.50	0.12
Co-m-Al_2O_3	3.3:3.2:2.6	3.5:3.4:2.7	0.53	0.53	0.02

Long-term stability studies and regeneration tests under industrially relevant reaction conditions are still scarce in the literature. Most of the reported results do not include regeneration studies or measurements longer than a few hours.[11,68,69,72,73] However, industrial applications require catalysts with stable performance over a longer time on stream with minimal activity and selectivity losses after regeneration. Thus, our catalytic tests are based on two long PDH cycles of each 24 h with an intermediate regeneration step (first 1 h in 5% and afterward 1 h in 20% oxygen).

It can be observed in Figure 3a that Co/γ-Al_2O_3, prepared by impregnation, had a higher initial activity but underwent fast deactivation within the first 10 h. The performance can be divided into two phases. During the initial phase, the propylene selectivity was increasing over time on stream, and the main side products were ethane and methane (Figure S14). Both side products were produced in a ratio close to one, suggesting that the hydrogenolysis of propane takes place. Hydrogenolysis is prone to take place on an active metal oxide in close proximity to Brønsted acid sites.[74,75] Our previous pyridine FTIR analysis corroborates that weak Brønsted centers are strong enough to promote hydrogenolysis since no strong Brønsted centers were found during the measurement at lower

temperatures and H_2 partial pressure. During the second phase, the propylene selectivity linearly decreases with ethylene and methane as the main byproducts. This indicates cracking of propane, which was reported to be independent of cobalt and taking place on the support.[44]

Moreover, the fast deactivation in the initial phase reveals that side reactions lead to blocking and/or modifications of active catalytic sites. However, Co-m-Al_2O_3 showed very different behavior (Figure 3a). Despite a lower initial propylene formation rate, the activity decreased by only 0.8 μmol g^{-1} s^{-1} for Co-m-Al_2O_3, with a constant high selectivity at around 95% vs 3.7 μmol g^{-1} s^{-1} for Co/γ-Al_2O_3. As a result, after 4 h of time on stream, Co-m-Al_2O_3 shows a higher propylene yield than Co/γ-Al_2O_3 with a notably lower deactivation rate due to the stability of the active sites. After the regeneration, both catalysts partially recovered their activity and showed a similar behavior as in the first cycle, evidencing that most active sites could be restored by oxidative treatment at 500 °C and a significant deactivation was caused by coke deposition. Nevertheless, Co-m-Al_2O_3 still showed superior performance in terms of high stability and propylene selectivity.
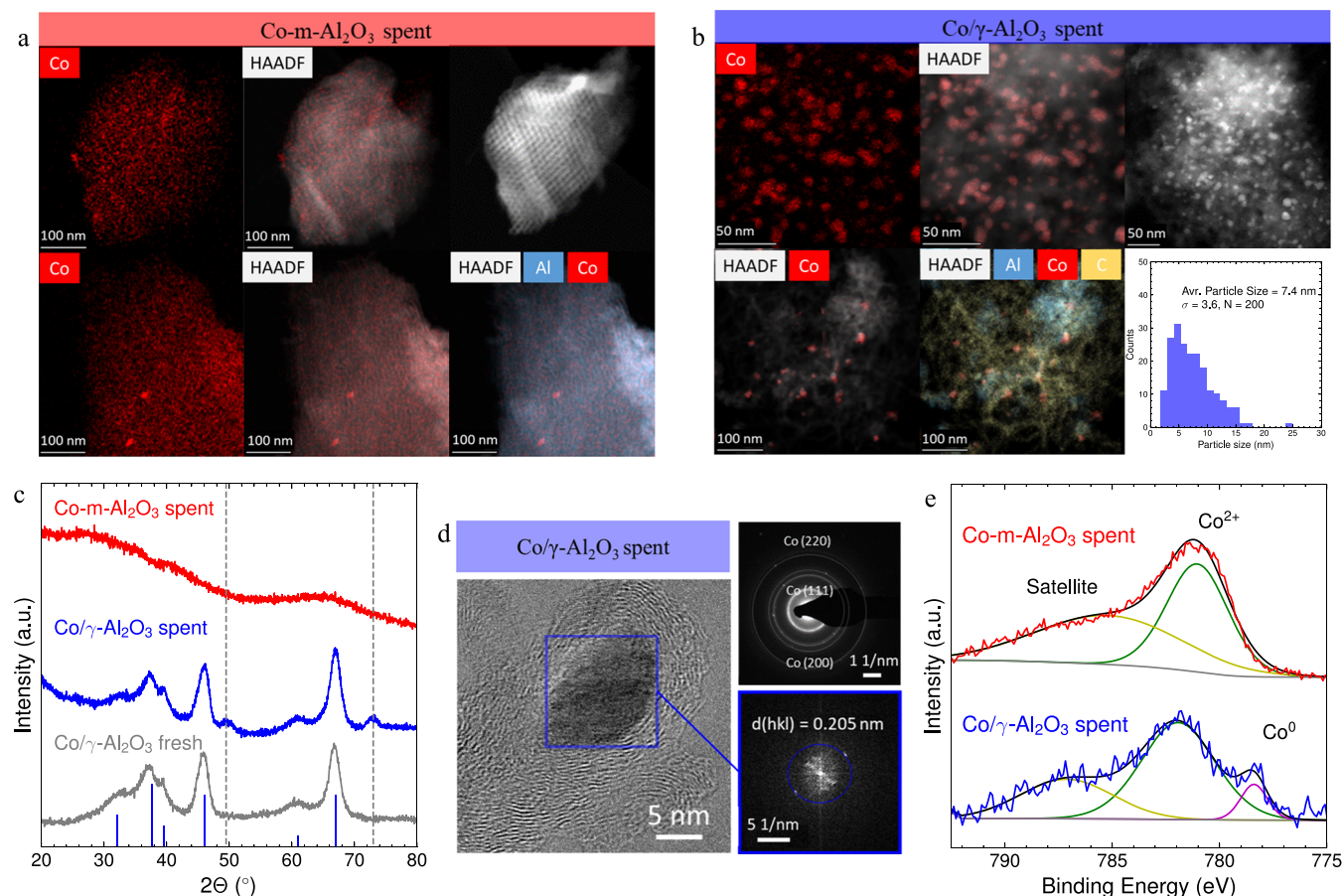
Figure 4. (a, b) STEM-EDS cobalt mapping of spent Co-m-Al$_2$O$_3$, Co/γ-Al$_2$O$_3$, and Co-m-Al$_2$O$_3$; (c) XRD pattern of spent cobalt catalysts after atmosphere contact and γ-Al$_2$O$_3$ reflexes (COD ID: 1531489); (d) HRTEM image of larger Co particle and the diffraction pattern (SAED) of spent Co/γ-Al$_2$O$_3$ with the inert transfer; and (e) XPS of Co 2p for spent catalysts with inert transfer (all after 12 h under reaction conditions).

The deactivation constants $k_{d,STY}$ and $k_{d,r}$ related to coke formation reveal distinct trends between Co-m-Al$_2$O$_3$ and Co/γ-Al$_2$O$_3$ (Table 2 and Figure S15). Co-m-Al$_2$O$_3$ showed a minor decrease in activity over time due to the deactivation of selective sites. In contrast, both selective and unselective sites exhibit decreased activity in Co/γ-Al$_2$O$_3$, where $k_{d,r}$ surpasses $k_{d,STY}$. However, the predominant activity loss in Co/γ-Al$_2$O$_3$ is attributed to the deactivation of selective sites. The coke-free deactivation constant $K_{d,r}$ markedly differs from $k_{d,STY}$ and $k_{d,r}$, underscoring coke formation as the main cause of quick deactivation in both catalysts. Additionally, a slower deactivation process arises from the sintering of cobalt particles. Notably, on the impregnated Co/γ-Al$_2$O$_3$, deactivation unrelated to coke deposition is 6 times more severe, suggesting significant sintering toward larger unselective cobalt particles.

For an objective comparison, an additional Pt−Sn−K/γ-Al$_2$O$_3$ catalyst was investigated, following the metal loading specifications outlined in a UOP LLC patent for a dehydrogenation catalyst composition.[2,6,8,24] The catalytic performance, along with synthesis details, is given in Figure S16. As can be seen, Pt−Sn−K/γ-Al$_2$O$_3$ shows higher activity compared to Co-based catalysts during the initial 12 h. However, its selectivity is notably lower and increases over time. Within just 12 h, propylene selectivity nearly reaches 90%. This increase in selectivity over time is attributed to coke deposition on the active but nonselective sites of Pt particles.[76] Consequently, the final selectivity of Pt−Sn−K/γ-Al$_2$O$_3$ falls

below that of Co-m-Al$_2$O$_3$, which remains constant at 95%. Similar to other Pt-based propane dehydrogenation catalysts, Pt−Sn−K/γ-Al$_2$O$_3$ also experiences evident deactivation.[2,8,9]

Figure 3b summarizes the reported cobalt catalysts tested in PDH. To establish a fair comparison, both the production rates of propylene per mass of cobalt and per mass of the catalyst, as well as the deactivation constants, are presented. Due to the limited availability of reported data, the space−time yield could only be compared after 1 and 5 h of TOS. The test conditions together with metal loadings are listed in Table S3 and Figure S17.[11,12,69,73,77−79] Remarkably, it can be seen that Co-m-Al$_2$O$_3$ possesses the highest STY per mass of cobalt and among the lowest deactivation rates reported to date. If the comparison is done only by the mass of the catalyst, a γ-Al$_2$O$_3$ sheet-shaped Co−Al$_2$O$_3$ catalyst reported by Dai et al.[12,78] showed similar or higher propylene production rates per mass of the catalyst and low deactivation. However, it is worth mentioning that Co-m-Al$_2$O$_3$ presented in this work contains 5 times less Co and could be compared after only 5 h of time on stream.

To gain a deeper understanding of the activity of cobalt, the effect of the support must also be considered. The role of the support in overall catalytic activity is often neglected in alkane dehydrogenation.[12,23,68,69,73,77−7879] Thus, the catalytic performance of γ-Al$_2$O$_3$ and m-Al$_2$O$_3$ supports is shown in Figure S18. γ-Al$_2$O$_3$ evidenced a higher activity than m-Al$_2$O$_3$ and a larger propylene formation rate. However, it can be seen for both cobalt-containing catalysts that the addition of cobalt notably increased both the activity and selectivity. After 12 h,

Co/γ-Al$_2$O$_3$ showed an identical performance to bare γ-Al$_2$O$_3$, while Co-m-Al$_2$O$_3$ was still significantly higher in activity and selectivity than m-Al$_2$O$_3$. This clearly suggests that the Co^{2+} sites on the impregnated catalyst deactivated comparably fast, and for longer reaction times, the reaction predominantly took place on the alumina support. In the first phase, the partly dispersed Co^{2+} promoted dehydrogenation, and the combination of Co^{2+} and weak Brønsted acid sites of γ-Al$_2$O$_3$ caused hydrogenolysis. In the second phase, when the catalytic process was driven by the support, mainly cracking was observed. Indeed, the main side products of bare γ-Al$_2$O$_3$ were C$_2$H$_4$ ($S_{C_2H_4}$(12 h) = 4.6%) and CH$_4$ (S_{CH_4}(12 h) = 3.5%), characteristic of the cracking reaction. Moreover, strong Lewis acid sites of the support are known to promote consecutive cracking of C−C bonds.[80] The comparably large number of strong Lewis acid sites on γ-Al$_2$O$_3$ can be correlated to the cracking side reactions (Figure 1e). Therefore, the lower selectivity is a result of the combination of large cobalt particles and the cracking properties of the γ-Al$_2$O$_3$ support.

In addition, cobalt was impregnated on bare m-Al$_2$O$_3$ (Co/m-Al$_2$O$_3$ (IWI)) and tested for PDH (Figure S18). The conversion and selectivity started identical to the one-pot EISA catalyst but deactivated severely within the first 2 h, while the selectivity stayed at 95%. This behavior suggests that although the selective Co^{2+} sites were initially present, they rapidly lost activity, unlike the stabilized Co^{2+} sites on Co-m-Al$_2$O$_3$. Nonetheless, the performance is still different from the bare support, indicating the activity of the remaining Co^{2+} sites.

Dispersion and Stability of Selective Cobalt Sites. The catalytic performance proved that a fine dispersion of Co^{2+} and incorporation in the ordered mesoporous alumina through a one-pot synthesis route could stabilize the selective and active sites in the PDH reaction. This is further confirmed by the analysis of the spent catalysts. Figure 4a shows the STEM-EDS of Co-m-Al$_2$O$_3$ after 12 h under reaction conditions. Remarkably, the catalyst preserved its high dispersion. Only a few large nanoparticles of up to 15 nm could be identified (Figure S19). However, most of the Co^{2+} remained highly dispersed. Also, the ordered mesoporous structure was preserved, as can be seen in the HAADF images.

In contrast, large Co^0 particles are observed on Co/γ-Al$_2$O$_3$ with an average particle size of 7.4 ± 3.5 nm (Figures 4b,c, S18 and S19). Consequently, larger metallic cobalt particles are formed under reaction conditions on the impregnated catalyst. Some of the particles are also detached from the alumina surface by formation of carbon nanotubes (Figures 4b, S20 and S21). It is reported that carbon nanotubes are preferably formed by larger metallic cobalt particles that lose activity over time.[81] Therefore, it can be ruled out that large metallic cobalt particles are inactive for dehydrogenation and responsible for carbon formation since Co/γ-Al$_2$O$_3$ shows the same activity as γ-Al$_2$O$_3$ after 12 h. An intermediate behavior could be observed for the impregnated Co/m-Al$_2$O$_3$ (IWI) catalyst, which lost activity fast in the first 2 h but showed higher activity and selectivity than the bare support. The average particle size on the spent catalyst is significantly smaller than on Co/γ-Al$_2$O$_3$ (Figure S21). Therefore, it can be assumed that some remaining small Co^{2+} nanoparticles are still active with a selectivity of 95% for propane dehydrogenation, while the formation of large cobalt particles reduces the conversion in the initial phase.

The dispersion for the spent catalysts was calculated following the criteria reported by Bergeret and Gallezot,[82] where values close to 0 correspond to a poor dispersion and values close to 1 represent a fine dispersion. For Co/γ-Al$_2$O$_3$, particles of 7.4 ± 3.6 nm give rise to a dispersion of 0.17. On the other hand, Co/m-Al$_2$O$_3$ (IWI) with an average particle size of 4.6 ± 2.6 nm results in a dispersion of 0.28. However, for particles smaller than 1.3 nm, the dispersion is larger than 0.99, as in the case of Co-m-Al$_2$O$_3$. Hence, a correlation between dispersion and propylene formation is established. It can be concluded from these observations that highly dispersed Co^{2+} shows the highest activity and selectivity for propane dehydrogenation. When metallic Co^0 particles are formed, the activity decreases. Consequently, these particles possess a lower activity. This decrease in activity continues as the particles grow under the reaction atmosphere.

In agreement with the STEM-EDS results, the same conclusions can be drawn from the *ex situ* XRD diffractograms of the spent catalysts after air contact (Figure 4d). Two additional peaks at 49.86 and 72.90° can be observed for the Co/γ-Al$_2$O$_3$ spent catalyst compared to the fresh sample. These peaks can be attributed to larger particles of oxidized cobalt particles. Metallic Co would show a main peak at ~47.4° and CoO at ~42.4°. Therefore, the peaks are ascribed to a mixed CoO$_x$ phase formed during the reaction and after air contact with the spent sample. Meanwhile, the spent Co-m-Al$_2$O$_3$ shows no additional peaks, confirming that the ordered mesoporous alumina preserved the high dispersion and prevented sintering and formation of larger cobalt particles even after 12 h of time on stream.

Nevertheless, the formation of large metallic Co^0 particles under reaction conditions was verified by HRTEM and XPS analysis of spent Co/γ-Al$_2$O$_3$ without contact with air (Figure 4d,e). Figure 4d shows an HRTEM micrograph of a large metallic cobalt particle surrounded by deposited carbon, together with the selected area diffraction pattern. The SAED fits well to the crystal structure of metallic cobalt with lattice planes (111) (0.205 nm), (200) (0.176 nm), and (220) (0.128 nm).[83,84] Additional HRTEM images are given in Figure S22. In agreement with the HRTEM for Co/γ-Al$_2$O$_3$, the XPS spectra showed an additional peak at 778.3 eV, showing the presence of metallic cobalt. This is not the case for Co-m-Al$_2$O$_3$, evidencing the high stability of Co^{2+} sites even after 12 h of time on stream.[54,55]

Therefore, it is concluded that the excellent stability of Co-m-Al$_2$O$_3$ results from the incorporation of well-dispersed Co^{2+} nanoclusters in the amorphous ordered mesoporous alumina. Meanwhile, support impregnations give rise to large Co^{2+} agglomerates at the surface acid sites. The reaction atmosphere is highly reductant, where larger cobalt agglomerates are easily reduced, as shown by Khodakov et al.[20,85,86] Co^{2+} is postulated as the selective site for the PDH reaction and the dispersion is of major importance, while large metallic Co^0 particles are unselective and prone to coking.[19,72] Therefore, it is shown that the small Co^{2+} species in Co-m-Al$_2$O$_3$ are active, stable, and selective toward propylene. Meanwhile, large particles on Co/γ-Al$_2$O$_3$ and Co/m-Al$_2$O$_3$ (IWI) are prone to be easily reduced, promoting undesired side reactions, like coking or hydrogenolysis.

Kinetics of Coke Formation: In Situ and Ex Situ Analyses. The most frequent causes of catalyst deactivation for propane dehydrogenation are sintering and blockage of the active sites due to coke formation.[87,88] As shown in the
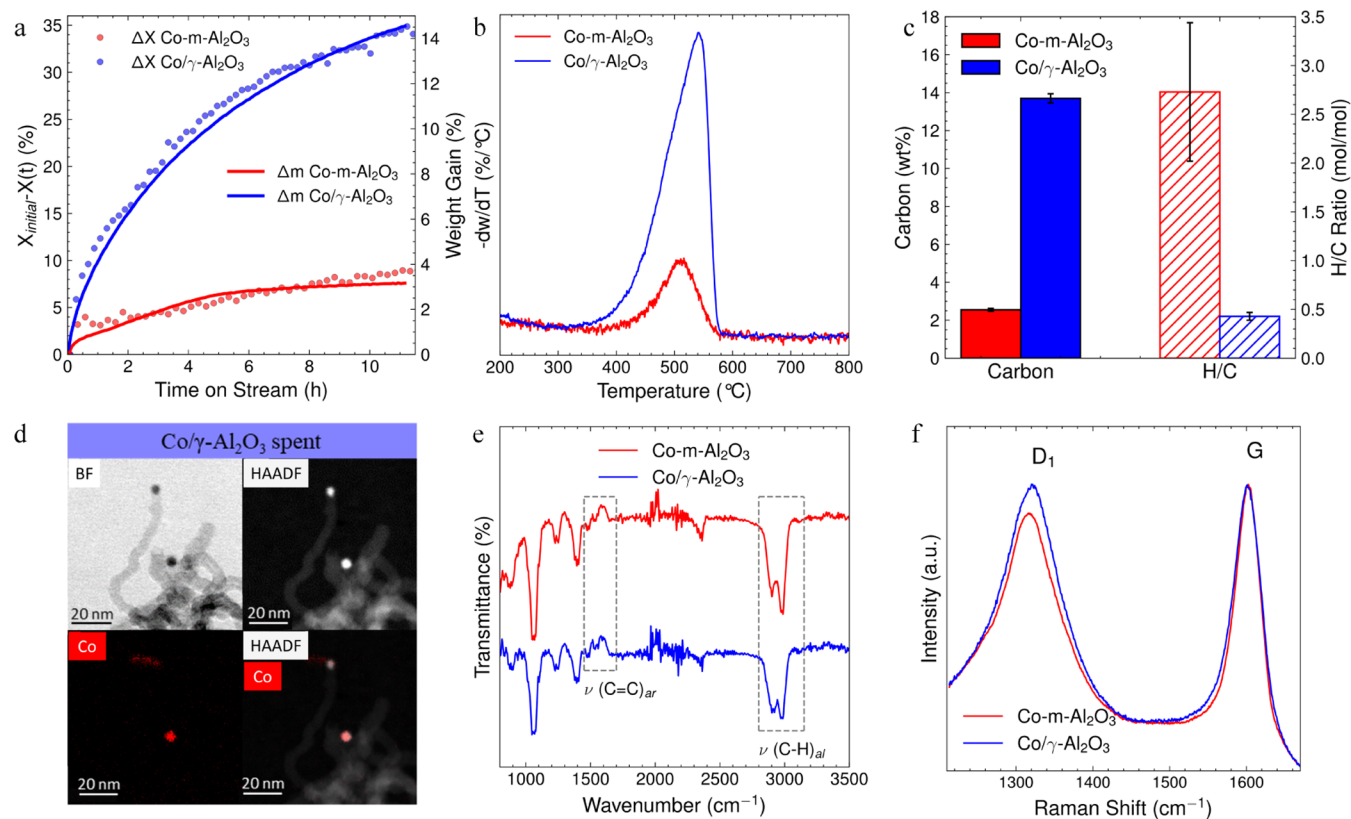
Figure 5. (a) In situ coke formation in a propane reaction atmosphere and activity decrease. (b) Derivative of the weight change during TPO of spent samples (12 h reaction). (c) Carbon content and the hydrogen−carbon ratio of spent catalysts identified by elemental analysis. (d) STEM-EDS cobalt mapping of carbon nanofibers on Co/γ-Al$_2$O$_3$. (e) IR transmittance of spent cobalt. (f) Raman spectra of coked catalysts with D$_1$ and G peak assignment.

catalytic performance, the comparison between the coke-containing and the coke-free deactivation constants ($k_{d,r}$ and $K_{d,r}$) suggests that the fast and strong activity loss at the beginning of the reaction is caused by coke formation. This section describes the interrelation of material properties to that of coking species.

Figure 5a (straight lines) depicts the thermal-gravimetric analysis of the catalysts under similar reaction conditions as the industrial Oleflex process. Remarkably, there is a clear difference in the kinetics of coke growth. Co/γ-Al$_2$O$_3$ forms coke comparably fast in the initial hours of the reaction, and the formation rate slowly decreases over time. Meanwhile, Co-m-Al$_2$O$_3$ only forms small amounts of coke in the initial 5 h. Afterward, almost no further coke is deposited on the catalytic surface. Figure 5a also showcases the activity loss (dotted lines, depicted as $X_{initial} - X_{(t)}$) together with the increase of deposited coke (straight lines, depicted as weight gain). Thus, the fast deactivation of Co/γ-Al$_2$O$_3$ (measured in the tubular reactor) is clearly correlated with the carbon deposition on the catalyst surface (measured *in situ* in the thermogravimetric balance under analogous PDH conditions). Therefore, it is evidenced that coke formation blocks the active sites, leading to activity loss.[78,89] Similarly, it can be observed that the Co-m-Al$_2$O$_3$ catalyst is able to suppress coke formation, in agreement with its stable catalytic performance and low deactivation.

It is known that the support can have a great influence on the coking behavior.[90] Specifically, strong Lewis acid sites are responsible for additional coke deposition.[91] Figure S23 shows the coke formation for the bare supports. While the bare m-Al$_2$O$_3$ practically does not contribute to coke formation, γ-

Al$_2$O$_3$ shows a steady coke growth rate, even after 12 h of time on stream. These results, together with the NH$_3$-TPD and pyridine FTIR studies, corroborate that strong Lewis acid sites on the alumina promote coke formation. As shown in the previous section, γ-Al$_2$O$_3$ has a noticeably larger amount of strong and medium Lewis acid sites. However, the alumina contribution is significantly lower in comparison with cobalt-containing catalysts, evidencing that the initial dispersion of Co^{2+}, in combination with the textural properties of the support, plays a pivotal role in the amount and kinetics of coke deposition.

Figures 5b,c show the coke content determined by TGA under an oxygen atmosphere and elemental analysis, respectively. The carbon content after the reaction was 2.5−3.5 wt % for Co-m-Al$_2$O$_3$ and 13.5−14.5 wt % for Co/γ-Al$_2$O$_3$. Thus, Co-m-Al$_2$O$_3$ catalysts prepared by the EISA route lead to 4.6 times less coke formation. The carbon content determined by the three different characterization techniques (TGA under PDH conditions, TPO, and elemental analysis) gives rise to the same quantity of coke (± 1 wt %). Thus, the kinetics studies derived from the thermogravimetric analysis under the PDH reaction are in excellent agreement with the catalytic results presented above. As can be observed in Figure 5b, coke oxidation starts at temperatures below 400 °C. Thus, the entire coke is burned during the regeneration process at 500 °C. As can be observed in the STEM-EDS images of the spent impregnated catalysts (Figures 5d, S20 and S21), part of the carbon is formed as carbon nanotubes from detached cobalt particles.[77] Since the particles are sitting on top of the constructed fiber, carbon nanotube formation follows a top-

Table 3. Peak Deconvolution Results from Raman Spectra Obtained from Three Different Points

sample	band	position (cm^{-1})	function	relative area (%)	$I(D_1)/I(G)$
Co-m-Al$_2$O$_3$	G	1602.4 ± 0.9	In Lorentzia	26.7 ± 0.9	0.84 ± 0.03
	D$_1$	1319.4 ± 1.2	In Lorentzia	60.5 ± 0.7	
	D$_3$	1515.5 ± 1.6	Gaussian	5.8 ± 0.1	
	D$_4$	1231.7 ± 2.1	In Lorentzia	6.9 ± 0.3	
Co/γ-Al$_2$O$_3$	G	1600.6 ± 0.7	In Lorentzia	25.0 ± 0.2	0.97 ± 0.02
	D$_1$	1319.1 ± 1.0	In Lorentzia	63.7 ± 1.0	
	D$_3$	1531.2 ± 1.3	Gaussian	5.3 ± 0.2	
	D$_4$	1226.5 ± 2.0	In Lorentzia	6.0 ± 1.0	

growth mechanism route, mainly caused by a weak cobalt support interaction.[92]

FTIR and Raman spectroscopies were applied for further study of the nature of deposited carbon. In the FTIR spectra (Figure 5e), several vibration bands can be observed between 800 and 3500 cm^{-1}. The significant vibration peaks from 2800 to 3100 cm^{-1} can be attributed to C−H symmetric and asymmetric stretching vibration from CH$_2$ and CH$_3$ groups.[93] This strong band indicated that the coke species contain significant amounts of hydrogen from aliphatic compounds, where the precursor is not entirely dehydrogenated. The aromatic compounds can be assigned to the peak at 1580 cm^{-1}, characteristic of C=C bonds.[93−95] The same wavelength vibration band is also observed for the presence of hexagonal carbon nanotubes, which were observed in the STEM images (Figure 5d). The coexistence of aliphatic and aromatic compounds (sp^3 and sp^2 hybridized carbon) is further evidenced by the bands at 1250 and 1515 cm^{-1}.[93,94] However, standard FTIR measurements are not suitable to distinguish between graphitic and aromatic coke since there are no significant peaks for pristine graphene. The spectrum also shows that there is no noticeable oxygen contamination in the carbon, which would result in bands at 1720 cm^{-1} (C−O and C=O) and 3400 cm^{-1} (O−H).[96]

Therefore, the coke deposited during the propane dehydrogenation is of aliphatic as well as aromatic/graphitic nature, where certain contributions of the aromatic/graphitic compounds are present as carbon nanotubes. In fact, the elemental analysis reveals a higher hydrogen-to-carbon ratio for Co-m-Al$_2$O$_3$ (Figure 5c). Thus, it is inferred that a larger aliphatic to aromatic/graphitic coke species ratio is present.[21] Indeed, considering the mechanism behind coke formation, it is demonstrated that the initial coke is often a contribution of aliphatic and aromatic products, while it grows into large aromatic and pregraphitic structures, resulting in a lower hydrogen-to-carbon ratio.[88,97]

Laser Raman spectroscopy allows a more detailed study of the nature of the carbon deposits. The spectra were evaluated by the method of Sadezky et al.,[98] as shown in Figure S24. The results of the deconvolution are listed in Table 3. The spectra for Co-m-Al$_2$O$_3$ and Co/γ-Al$_2$O$_3$ in Figure 5f show similar main bands with peaks at ~1320 and ~1601 cm^{-1}. However, the D$_1$ band has a larger intensity for Co/γ-Al$_2$O$_3$. Consequently, the $I(D_1)/I(G)$ ratio increases. Together with a slight shift of the G peak and a smaller D$_3$ area, the larger $I(D_1)/I(G)$ ratio suggests a higher degree of graphitization and a lower impact from sp^3 chain-type structures.[99−101] As shown by Ferrari et al., in the regime of amorphous carbon, the development of the D peak indicates ordering.[100,101] Therefore, the ratio of amorphous carbon is larger on Co-m-Al$_2$O$_3$, in agreement with elemental analysis and FTIR measurements.

In summary, under reaction conditions, Co/γ-Al$_2$O$_3$ accumulates a larger amount of coke with faster kinetics on the catalyst surface. Both cobalt catalysts have aliphatic, aromatic, and (pre)graphitic coke species, but Co-m-Al$_2$O$_3$ shows a lower degree of graphitization with a larger quantity of aliphatic species.

■ CONCLUSIONS

In this study, highly dispersed Co^{2+} nanoclusters could be stabilized in ordered mesoporous alumina supports by a simple sol−gel route, following the one-pot evaporation-induced self-assembly method. The amorphous ordered mesoporous structure of the alumina is preserved after long-term studies of propane dehydrogenation and regeneration under industrially relevant Oleflex conditions. The results from XRD, XPS, STEM-EDS, UV−vis, X-ray absorption, ^{27}Al-MAS NMR, and NH$_3$-TPD studies of the pristine catalyst clearly indicate that the cobalt is incorporated into the structure of the ordered mesoporous alumina, leading to very small and well-dispersed Co^{2+} clusters below 1 nm showing tetrahedral coordination. The cobalt nanoclusters are remarkably stable under reaction conditions, resulting in low deactivation and high and stable propylene selectivity. This underlines the beneficial cobalt bonding within the m-Al$_2$O$_3$ structure instead of weaker interactions with the acid sites on the surface.

Alumina with impregnated cobalt (Co/γ-Al$_2$O$_3$ and Co/m-Al$_2$O$_3$ (IWI)) strongly deactivates with fast coke formation and/or formation of large metallic particles. Cobalt particles with a mean size of 7.4 nm were formed in 12 h under reaction conditions on Co/γ-Al$_2$O$_3$ and 14 wt % of coke was accumulated. This leads to a loss of 65.4% of the initial space−time yield. The deactivation is ascribed to the weaker Co^{2+}−support interaction, leading to the formation of larger cobalt particles, as well as strong acid sites of the support, promoting the formation of carbon layers and carbon nanotubes under reaction conditions. These findings unravel structure−performance correlations on the nature of cobalt and support sites applied for propane dehydrogenation, useful for the design of stable dehydrogenation catalysts applied under harsh conditions.

■ ASSOCIATED CONTENT

Ⓢ Supporting Information

The Supporting Information is available free of charge at https://pubs.acs.org/doi/10.1021/acscatal.4c02067.

TG analysis; XRD patterns; TEM images; SAX pattern; nitrogen isotherms; ^{27}Al-NMR signals; NH$_3$-TPD profiles; STEM-EDS mappings; XPS; catalytic performance; literature data; HRTEM images; and Raman spectra (PDF)

AUTHOR INFORMATION

Corresponding Author

Esteban Gioria − *BasCat—UniCat BASF JointLab, Technical University of Berlin, Berlin 10623, Germany; Functional Materials, Department of Chemistry, Technische Universität Berlin, Berlin 10623, Germany; Present Address: Surface Science and Catalysis (SurfCat), Department of Physics, Technical University of Denmark, 2800 Kongens Lyngby, Denmark;* orcid.org/0000-0001-6918-5734; Email: egagi@dtu.dk

Authors

Fabian Ebert − *BasCat—UniCat BASF JointLab, Technical University of Berlin, Berlin 10623, Germany*

Piyush Ingale − *BasCat—UniCat BASF JointLab, Technical University of Berlin, Berlin 10623, Germany; R&D Solutions, hte GmbH—The High Throughput Experimentation Company, Heidelberg 69123, Germany*

Sarah Vogl − *Functional Materials, Department of Chemistry, Technische Universität Berlin, Berlin 10623, Germany*

Sebastian Praetz − *Analytical X-ray Physics, Institute of Optics and Atomic Physics, Technical University of Berlin, Berlin 10623, Germany;* orcid.org/0000-0001-6852-7616

Christopher Schlesiger − *Analytical X-ray Physics, Institute of Optics and Atomic Physics, Technical University of Berlin, Berlin 10623, Germany*

Nils Pfister − *Interface Science Department, Fritz Haber Institut/Max Planck Society, Berlin 12489, Germany*

Raoul Naumann d'Alnoncourt − *BasCat—UniCat BASF JointLab, Technical University of Berlin, Berlin 10623, Germany;* orcid.org/0000-0002-9946-4619

Beatriz Roldán Cuenya − *Interface Science Department, Fritz Haber Institut/Max Planck Society, Berlin 12489, Germany;* orcid.org/0000-0002-8025-307X

Arne Thomas − *Functional Materials, Department of Chemistry, Technische Universität Berlin, Berlin 10623, Germany;* orcid.org/0000-0002-2130-4930

Frank Rosowski − *BasCat—UniCat BASF JointLab, Technical University of Berlin, Berlin 10623, Germany; BASF SE, Ludwigshafen 67056, Germany*

Complete contact information is available at:
https://pubs.acs.org/10.1021/acscatal.4c02067

Notes

The authors declare no competing financial interest.

REFERENCES

(1) Sattler, J. J. H. B.; Ruiz-Martinez, J.; Santillan-Jimenez, E.; Weckhuysen, B. M. Catalytic Dehydrogenation of Light Alkanes on Metals and Metal Oxides. *Chem. Rev.* **2014**, *114* (20), 10613−10653.

(2) Chen, S.; Chang, X.; Sun, G.; Zhang, T.; Xu, Y.; Wang, Y.; Pei, C.; Gong, J. Propane Dehydrogenation: Catalyst Development, New Chemistry, and Emerging Technologies. *Chem. Soc. Rev.* **2021**, *50* (5), 3315−3354.

(3) James, O. O.; Mandal, S.; Alele, N.; Chowdhury, B.; Maity, S. Lower Alkanes Dehydrogenation: Strategies and Reaction Routes to Corresponding Alkenes. *Fuel Process. Technol.* **2016**, *149*, 239−255.

(4) Kim, S.; Jeong, S.; Heo, E. Effects of the Shale Boom on Ethylene and Propylene Prices. *Energy Sources, Part B* **2019**, *14* (3), 49−66.

(5) Monai, M.; Gambino, M.; Wannakao, S.; Weckhuysen, B. M. Propane to Olefins Tandem Catalysis: A Selective Route towards Light Olefins Production. *Chem. Soc. Rev.* **2021**, *50* (20), 11503−11529.

(6) Samanta, C.; Das, R. K.C3-Based Petrochemicals: Recent Advances in Processes and Catalysts. In *Catalysis for Clean Energy and Environmental Sustainability*; Springer, 2021; pp 149−204.

(7) Vora, B. V. Development of Dehydrogenation Catalysts and Processes. *Top. Catal.* **2012**, *55* (19−20), 1297−1308.

(8) Sun, M. L.; Hu, Z. P.; Wang, H. Y.; Suo, Y. J.; Yuan, Z. Y. Design Strategies of Stable Catalysts for Propane Dehydrogenation to Propylene. *ACS Catal.* **2023**, *13*, 4719−4741.

(9) Ingale, P.; Knemeyer, K.; Preikschas, P.; Ye, M.; Geske, M.; d'Alnoncourt, R. N.; Thomas, A.; Rosowski, F. Design of PtZn Nanoalloy Catalysts for Propane Dehydrogenation through Interface Tailoringviaatomic Layer Deposition. *Catal. Sci. Technol.* **2021**, *11* (2), 484−493.

(10) Anderson, D. L. Chemical Composition of the Mantle. In *Theory of Earth*; Blackwell Scientific Publications: Boston, 1998.

(11) Bian, Z.; Dewangan, N.; Wang, Z.; Pati, S.; Xi, S.; Borgna, A.; Kus, H.; Kawi, S. Mesoporous-Silica-Stabilized Cobalt(II) Oxide Nanoclusters for Propane Dehydrogenation. *ACS Appl. Nano Mater.* **2021**, *4* (2), 1112−1125.

(12) Dai, Y.; Gu, J.; Tian, S.; Wu, Y.; Chen, J.; Li, F.; Du, Y.; Peng, L.; Ding, W.; Yang, Y. γ-Al2O3 Sheet-Stabilized Isolate Co2+ for Catalytic Propane Dehydrogenation. *J. Catal.* **2020**, *381*, 482−492.

(13) Gao, Y.; Peng, L.; Long, J.; Wu, Y.; Dai, Y.; Yang, Y. Hydrogen Pre−Reduction Determined Co−Silica Interaction and Performance of Cobalt Catalysts for Propane Dehydrogenation. *Microporous Mesoporous Mater.* **2021**, *323*, No. 111187.

(14) Sui, X.; Zhang, L.; Li, J.; Doyle-Davis, K.; Li, R.; Wang, Z.; Sun, X. Advanced Support Materials and Interactions for Atomically Dispersed Noble-Metal Catalysts: From Support Effects to Design Strategies. *Adv. Energy Mater.* **2022**, *12* (1), No. 2102556.

(15) Zhang, L.; Doyle-Davis, K.; Sun, X. Pt-Based Electrocatalysts with High Atom Utilization Efficiency: From Nanostructures to Single Atoms. *Energy Environ. Sci.* **2019**, *12* (2), 492−517.

(16) Rochlitz, L.; Searles, K.; Alfke, J.; Zemlyanov, D.; Safonova, O. V.; Copéret, C. Silica-Supported, Narrowly Distributed, Subnanometric Pt-Zn Particles from Single Sites with High Propane Dehydrogenation Performance. *Chem. Sci.* **2020**, *11* (6), 1549−1555.

(17) Liu, L.; Corma, A. Metal Catalysts for Heterogeneous Catalysis: From Single Atoms to Nanoclusters and Nanoparticles. *Chem. Rev.* **2018**, *118* (10), 4981−5079.

(18) den Breejen, J. P.; Radstake, P. B.; Bezemer, G. L.; Bitter, J. H.; Frøseth, V.; Holmen, A.; de Jong, K. P. On the Origin of the Cobalt Particle Size Effects in Fischer−Tropsch Catalysis. *J. Am. Chem. Soc.* **2009**, *131* (20), 7197−7203.

(19) Li, X.; Wang, P.; Wang, H.; Li, C. Effects of the State of Co Species in Co/Al 2 O 3 Catalysts on the Catalytic Performance of Propane Dehydrogenation. *Appl. Surf. Sci.* **2018**, *441*, 688−693.

(20) Khodakov, A. Y.; Griboval-Constant, A.; Bechara, R.; Villain, F. Pore-Size Control of Cobalt Dispersion and Reducibility in Mesoporous Silicas. *J. Phys. Chem. B* **2001**, *105* (40), 9805−9811.

(21) Wang, H. Z.; Sun, L. L.; Sui, Z. J.; Zhu, Y. A.; Ye, G. H.; Chen, D.; Zhou, X. G.; Yuan, W. K. Coke Formation on Pt-Sn/Al2O3 Catalyst for Propane Dehydrogenation. *Ind. Eng. Chem. Res.* **2018**, *57* (26), 8647−8654.

(22) Macêdo, M. I. F.; Bertran, C. A.; Osawa, C. C. Kinetics of the $\gamma \rightarrow \alpha$-Alumina Phase Transformation by Quantitative X-Ray Diffraction. *J. Mater. Sci.* **2007**, *42* (8), 2830−2836.

(23) Zhang, H.; Jiang, Y.; Wang, G.; Tang, N.; Zhu, X.; Li, C.; Shan, H. In-Depth Study on Propane Dehydrogenation over Al2O3-Based Unconventional Catalysts with Different Crystal Phases. *Mol. Catal.* **2022**, *519*, No. 112143.

(24) Voskoboynikov, T. V.; Wei, D. H.; Sachtler, J. W. A.; Vora, B. V. Dehydrogenation Catalyst Composition. U.S. Patent US6,756,340B2, 2004.

(25) Maddah, H. A. A Comparative Study between Propane Dehydrogenation (PDH) Technologies and Plants in Saudi Arabia. *Am. Sci. Res. J. Eng. Technol. Sci.* **2018**, *45* (1), 49−63.

(26) Yang, F.; Zhang, J.; Shi, Z.; Chen, J.; Wang, G.; He, J.; Zhao, J.; Zhuo, R.; Wang, R. Advanced Design and Development of Catalysts in Propane Dehydrogenation. *Nanoscale* **2022**, *14* (28), 9963−9988.

(27) Lian, Z.; Si, C.; Jan, F.; Zhi, S.; Li, B. Coke Deposition on Pt-Based Catalysts in Propane Direct Dehydrogenation: Kinetics, Suppression, and Elimination. *ACS Catal.* **2021**, *11* (15), 9279−9292.

(28) Schlesiger, C.; Anklamm, L.; Stiel, H.; Malzer, W.; Kanngießer, B. XAFS Spectroscopy by an X-Ray Tube Based Spectrometer Using a Novel Type of HOPG Mosaic Crystal and Optimized Image Processing. *J. Anal. At. Spectrom.* **2015**, *30* (5), 1080−1085.

(29) Schlesiger, C.; Praetz, S.; Gnewkow, R.; Malzer, W.; Kanngießer, B. Recent Progress in the Performance of HAPG Based Laboratory EXAFS and XANES Spectrometers. *J. Anal. At. Spectrom.* **2020**, *35* (10), 2298−2304.

(30) Ravel, B.; Newville, M. ATHENA, ARTEMIS, HEPHAESTUS: Data Analysis for X-Ray Absorption Spectroscopy Using IFEFFIT. *J. Synchrotron Radiat.* **2005**, *12* (4), 537−541.

(31) Gioria, E.; Ingale, P.; Pohl, F.; d'Alnoncourt, R. N.; Thomas, A.; Rosowski, F. Boosting the Performance of Ni/Al 2 O 3 for the Reverse Water Gas Shift Reaction through Formation of CuNi Nanoalloys. *Catal. Sci. Technol.* **2022**, *12* (2), 474−487.

(32) Yuan, Q.; Yin, A. X.; Luo, C.; Sun, L. D.; Zhang, Y. W.; Duan, W. T.; Liu, H. C.; Yan, C. H. Facile Synthesis for Ordered Mesoporous γ-Aluminas with High Thermal Stability. *J. Am. Chem. Soc.* **2008**, *130* (11), 3465−3472.

(33) Tang, N.; Cong, Y.; Shang, Q.; Wu, C.; Xu, G.; Wang, X. Coordinatively Unsaturated Al3+ Sites Anchored Subnanometric Ruthenium Catalyst for Hydrogenation of Aromatics. *ACS Catal.* **2017**, *7* (9), 5987−5991.

(34) Kwak, J. H.; Hu, J.; Mei, D.; Yi, C.-W.; Kim, D. H.; Peden, C. H. F.; Allard, L. F.; Szanyi, J. Coordinatively Unsaturated Al3+ Centers as Binding Sites for Active Catalyst of Platinum on Gamma-Al2O3. *Science* **2009**, *325* (5948), 1670−1673.

(35) Yang, X.; Li, Q.; Lu, E.; Wang, Z.; Gong, X.; Yu, Z.; Guo, Y.; Wang, L.; Guo, Y.; Zhan, W.; Zhang, J.; Dai, S. Taming the Stability of Pd Active Phases through a Compartmentalizing Strategy toward Nanostructured Catalyst Supports. *Nat. Commun.* **2019**, *10* (1), No. 1611.

(36) Shi, L.; Deng, G.; Li, W.; Miao, S.; Wang, Q.; Zhang, W.; Lu, A. Al 2 O 3 Nanosheets Rich in Pentacoordinate Al 3+ Ions Stabilize Pt-Sn Clusters for Propane Dehydrogenation. *Angew. Chem.* **2015**, *127* (47), 14200−14204.

(37) Han, W.; Liu, B.; Chen, Y.; Jia, Z.; Wei, X.; Song, W. Coordinatively Unsaturated Aluminum Anchored Ru Cluster for Catalytic Hydrogenation of Benzene. *J. Catal.* **2021**, *400*, 255−264.

(38) Li, Z.; Jiang, Y.; Zhou, R.; Chen, Z.; Shan, Q.; Tan, J. Effect of Cr Addition on the Microstructure and Abrasive Wear Resistance of WC-Reinforced Iron Matrix Surface Composites. *J. Mater. Res.* **2014**, *29* (6), 778−785.

(39) Yu, F.; Bi, S.; Liu, T.; Pan, D.; Chen, S.; Yan, X.; Fan, B.; Li, R. Synthesis of Ordered Mesoporous Zr-al Composite Oxides with Excellent Structural and Textural Properties and Extremely High Stability. *Materials* **2020**, *13* (13), No. 3036.

(40) Pan, D.; Xu, Q.; Dong, Z.; Chen, S.; Yu, F.; Yan, X.; Fan, B.; Li, R. Facile Synthesis of Highly Ordered Mesoporous Cobalt-Alumina Catalysts and Their Application in Liquid Phase Selective Oxidation of Styrene. *RSC Adv.* **2015**, *5* (119), 98377−98390.

(41) Pan, D.; Chen, W.; Huang, X.; Zhang, J.; Yang, Y.; Yu, F.; Chen, S.; Fan, B.; Shi, X.; Cui, X.; Li, R.; Yu, C. Solvothermal-Assisted Evaporation-Induced Self-Assembly of Ordered Mesoporous Alumina with Improved Performance. *J. Colloid Interface Sci.* **2018**, *529*, 432−443.

(42) Yue, Y.; Fu, J.; Wang, C.; Yuan, P.; Bao, X.; Xie, Z.; Basset, J. M.; Zhu, H. Propane Dehydrogenation Catalyzed by Single Lewis Acid Site in Sn-Beta Zeolite. *J. Catal.* **2021**, *395*, 155−167.

(43) Lin, G.; Su, Y.; Duan, X.; Xie, K. High-Density Lewis Acid Sites in Porous Single-Crystalline Monoliths to Enhance Propane Dehydrogenation at Reduced Temperatures. *Angew. Chem., Int. Ed.* **2021**, *60* (17), 9311−9315.

(44) Yu, S. Y.; Yu, G. J.; Li, W.; Iglesia, E. Kinetics and Reaction Pathways for Propane Dehydrogenation and Aromatization on Co/H-ZSM5 and H-ZSM5. *J. Phys. Chem. B* **2002**, *106* (18), 4714−4720.

(45) Zhang, Y.; Zhou, Y.; Sheng, X.; Wan, L.; Li, Y.; Xiao, Y.; Yu, B.; Zeng, Z. Effect of the Competitive Adsorbates on the Catalytic Performances of PtSnK/γ-Al 2O 3 Catalyst for Isobutane Dehydrogenation. *Fuel Process. Technol.* **2012**, *104*, 23−30.

(46) Wannaborworn, M.; Praserthdam, P.; Jongsomjit, B. A Comparative Study of Solvothermal and Sol-Gel-Derived Nanocrystalline Alumina Catalysts for Ethanol Dehydration. *J. Nanomater.* **2015**, *2015*, No. 519425.

(47) Katada, N.; Igi, H.; Kim, J.-H.; Niwa, M. Determination of the Acidic Properties of Zeolite by Theoretical Analysis of Temperature-Programmed Desorption of Ammonia Based on Adsorption Equilibrium. *J. Phys. Chem. B* **1997**, *101* (31), 5969−5977.

(48) Niwa, M.; Katada, N. Measurements of Acidic Property of Zeolites by Temperature Programmed Desorption of Ammonia. *Catal. Surv. Jpn.* **1997**, *1*, 215−226.

(49) Masuda, T.; Fujikata, Y.; Mukai, S. R.; Hashimoto, K. A Method of Calculating Adsorption Enthalpy Distribution Using Ammonia Temperature-Programmed Desorption Spectrum under Adsorption Equilibrium Conditions. *Appl. Catal., A* **1997**, *165*, 57−72.

(50) Tamura, M.; Shimizu, K. I.; Satsuma, A. Comprehensive IR Study on Acid/Base Properties of Metal Oxides. *Appl. Catal., A* **2012**, *433−434*, 135−145.

(51) Moroz, I. B.; Larmier, K.; Liao, W. C.; Copéret, C. Discerning γ-Alumina Surface Sites with Nitrogen-15 Dynamic Nuclear Polarization Surface Enhanced NMR Spectroscopy of Adsorbed Pyridine. *J. Phys. Chem. C* **2018**, *122* (20), 10871−10882.

(52) Morterra, C.; Chiorino, A.; Ghiotti, G.; Garrone, E. Surface Acidity of η-Alumina. Part 1.-Pyridine Chemisorption at Room Temperature. *J. Chem. Soc., Faraday Trans. 1* **1979**, *75*, 271−288.

(53) Ghosh, M.; Sampathkumaran, E. V.; Rao, C. N. R. Synthesis and Magnetic Properties of CoO Nanoparticles. *Chem. Mater.* **2005**, *17* (9), 2348−2352.

(54) Ohyama, J.; Abe, D.; Hirayama, A.; Iwai, H.; Tsuchimura, Y.; Sakamoto, K.; Irikura, M.; Nakamura, Y.; Yoshida, H.; Machida, M.; Nishimura, S.; Yamamoto, T.; Matsumura, S.; Takahashi, K. Selective Oxidation of Methane to Formaldehyde over a Silica-Supported Cobalt Single-Atom Catalyst. *J. Phys. Chem. C* **2022**, *126* (4), 1785−1792.

(55) Chuang, T. J.; Bridle, C. R.; Rice, D. W. Interpretation of the X-Ray Photoemission Spectra of Cobalt Oxides and Cobalt Oxide Surface. *Surf. Sci.* **1976**, *59*, 413−429.

(56) Taguchi, M.; Nakane, T.; Hashi, K.; Ohki, S.; Shimizu, T.; Sakka, Y.; Matsushita, A.; Abe, H.; Funazukuri, T.; Naka, T. Reaction Temperature Variations on the Crystallographic State of Spinel Cobalt Aluminate. *Dalton Trans.* **2013**, *42* (19), 7167−7176.

(57) Zayat, M.; Levy, D. Blue CoAl2O4 Particles Prepared by the Sol-Gel and Citrate-Gel Methods. *Chem. Mater.* **2000**, *12* (9), 2763−2769.

(58) He, T.; Becker, K. D. An Optical In-Situ Study of a Reacting Spinel Crystal. *Solid State Ionics* **1997**, *101−103*, 337−342.

(59) Cui, H.; Zhang, Y.; Qiu, Z.; Zhao, L.; Zhu, Y. Synthesis and Characterization of Cobalt-Substituted SBA-15 and Its High Activity in Epoxidation of Styrene with Molecular Oxygen. *Appl. Catal., B* **2010**, *101* (1−2), 45−53.

(60) Herrero, M.; Benito, P.; Labajos, F. M.; Rives, V. Stabilization of Co2+ in Layered Double Hydroxides (LDHs) by Microwave-Assisted Ageing. *J. Solid State Chem.* **2007**, *180* (3), 873−884.

(61) Kurajica, S.; Popović, J.; Tkalčec, E.; Gržeta, B.; Mandić, V. The Effect of Annealing Temperature on the Structure and Optical Properties of Sol-Gel Derived Nanocrystalline Cobalt Aluminate Spinel. *Mater. Chem. Phys.* **2012**, *135* (2−3), 587−593.

(62) Molinari, C.; Conte, S.; Zanelli, C.; Ardit, M.; Cruciani, G.; Dondi, M. Ceramic Pigments and Dyes beyond the Inkjet Revolution: From Technological Requirements to Constraints in Colorant Design. *Ceram. Int.* **2020**, *46* (14), 21839−21872.

(63) Kim, M. G.; Yo, C. H. X-Ray Absorption Spectroscopic Study of Chemically and Electrochemically Li Ion Extracted LiyCo0.85Al0.15O2 Compounds. *J. Phys. Chem. B* **1999**, *103* (31), 6457−6465.

(64) Gajdek, D.; Olsson, P. A. T.; Blomberg, S.; Gustafson, J.; Carlsson, P. A.; Haase, D.; Lundgren, E.; Merte, L. R. Structural Changes in Monolayer Cobalt Oxides under Ambient Pressure CO and O2 Studied by in Situ Grazing-Incidence X-Ray Absorption Fine Structure Spectroscopy. *J. Phys. Chem. C* **2022**, *126* (7), 3411−3418.

(65) Maurizio, C.; Habra, N. E.; Rossetto, G.; Merlini, M.; Cattaruzza, E.; Pandolfo, L.; Casarin, M. XAS and GIXRD Study of Co Sites in CoAl2O4 Layers Grown by MOCVD. *Chem. Mater.* **2010**, *22* (5), 1933−1942.

(66) Wei, C.; Feng, Z.; Scherer, G. G.; Barber, J.; Shao-Horn, Y.; Xu, Z. J. Cations in Octahedral Sites: A Descriptor for Oxygen Electrocatalysis on Transition-Metal Spinels. *Adv. Mater.* **2017**, *29* (23), No. 1606800.

(67) Koirala, R.; Safonova, O. V.; Pratsinis, S. E.; Baiker, A. Effect of Cobalt Loading on Structure and Catalytic Behavior of CoOx/SiO2 in CO2-Assisted Dehydrogenation of Ethane. *Appl. Catal., A* **2018**, *552*, 77−85.

(68) Hu, B.; Kim, W. G.; Sulmonetti, T. P.; Sarazen, M. L.; Tan, S.; So, J.; Liu, Y.; Dixit, R. S.; Nair, S.; Jones, C. W. A Mesoporous Cobalt Aluminate Spinel Catalyst for Nonoxidative Propane Dehydrogenation. *ChemCatChem* **2017**, *9* (17), 3330−3337.

(69) Zhao, Y.; Sohn, H.; Hu, B.; Niklas, J.; Poluektov, O. G.; Tian, J.; Delferro, M.; Hock, A. S. Zirconium Modification Promotes Catalytic Activity of a Single-Site Cobalt Heterogeneous Catalyst for Propane Dehydrogenation. *ACS Omega* **2018**, *3* (9), 11117−11127.

(70) Samanta, C.; Das, R. K. *Catalysis for Clean Energy and Environmental Sustainability*; Springer International Publishing, 2021. DOI: 10.1007/978-3-030-65021-6.

(71) Cottrell, P. R.; Fettis, M. E. Process for Dehydrogenation of Hydrocarbons.U.S. Patent US005,087,792A, 1992.

(72) Hu, B.; Getsoian, A. B.; Schweitzer, N. M.; Das, U.; Kim, H.; Niklas, J.; Poluektov, O.; Curtiss, L. A.; Stair, P. C.; Miller, J. T.; Hock, A. S. Selective Propane Dehydrogenation with Single Site CoII on SiO2 by a Non-Redox Mechanism. *J. Catal.* **2015**, *322*, 24−37.

(73) Huang, Z.; He, D.; Deng, W.; Jin, G.; Li, K.; Luo, Y. Illustrating New Understanding of Adsorbed Water on Silica for Inducing Tetrahedral Cobalt(II) for Propane Dehydrogenation. *Nat. Commun.* **2023**, *14* (1), No. 100.

(74) Arzumanov, S. S.; Gabrienko, A. A.; Toktarev, A. V.; Lashchinskaya, Z. N.; Freude, D.; Haase, J.; Stepanov, A. G. Propane Transformation on Zn-Modified Zeolite. Effect of the Nature of Zn

Species on Alkane Aromatization and Hydrogenolysis. *J. Phys. Chem. C* **2019**, *123* (50), 30473−30485.

(75) Gabrienko, A. A.; Arzumanov, S. S.; Freude, D.; Stepanov, A. G. Propane Aromatization on Zn-Modified Zeolite Bea Studied by Solid-State NMR in Situ. *J. Phys. Chem. C* **2010**, *114* (29), 12681−12688.

(76) Kaylor, N.; Davis, R. J. Propane Dehydrogenation over Supported Pt-Sn Nanoparticles. *J. Catal.* **2018**, *367*, 181−193.

(77) Dewangan, N.; Ashok, J.; Sethia, M.; Das, S.; Pati, S.; Kus, H.; Kawi, S. Cobalt-Based Catalyst Supported on Different Morphologies of Alumina for Non-Oxidative Propane Dehydrogenation: Effect of Metal Support Interaction and Lewis Acidic Sites. *ChemCatChem* **2019**, *11* (19), 4923−4934.

(78) Dai, Y.; Wu, Y.; Dai, H.; Gao, X.; Tian, S.; Gu, J.; Yi, X.; Zheng, A.; Yang, Y. Effect of Coking and Propylene Adsorption on Enhanced Stability for Co2+-Catalyzed Propane Dehydrogenation. *J. Catal.* **2021**, *395*, 105−116.

(79) Sun, Y.; Wu, Y.; Shan, H.; Li, C. Studies on the Nature of Active Cobalt Species for the Production of Methane and Propylene in Catalytic Dehydrogenation of Propane. *Catal. Lett.* **2015**, *145* (7), 1413−1419.

(80) Lee, M. H.; Nagaraja, B. M.; Natarajan, P.; Truong, N. T.; Lee, K. Y.; Yoon, S.; Jung, K. D. Effect of Potassium Addition on Bimetallic PtSn/*θ*-Al2O3 Catalyst for Dehydrogenation of Propane to Propylene. *Res. Chem. Intermed.* **2016**, *42* (1), 123−140.

(81) Takenaka, S.; Ishida, M.; Serizawa, M.; Tanabe, E.; Otsuka, K. Formation of Carbon Nanofibers and Carbon Nanotubes through Methane Decomposition over Supported Cobalt Catalysts. *J. Phys. Chem. B* **2004**, *108* (31), 11464−11472.

(82) Bergeret, G.; Gallezot, P. *Particle Size and Dispersion Measurements. Handbook of Heterogeneous Catalysis*; Wiley-VCH, 2008; Vol. 2.

(83) Owen, E. A.; Jones, D. M. Effect of Grain Size on the Crystal Structure of Cobalt. *Proc. Phys. Soc., Sect. B* **1954**, *67* (6), 456.

(84) Marick, L. Variation of Resistance and Structure of Cobalt with Temperature and a Discussion of Its Photoelectric Emission. *Phys. Rev.* **1936**, *49* (11), No. 831.

(85) Lendzion-Bieluń, Z.; Jędrzejewski, R.; Arabczyk, W. The Effect of Aluminium Oxide on the Reduction of Cobalt Oxide and Thermostabillity of Cobalt and Cobalt Oxide. *Open Chem.* **2011**, *9* (5), 834−839.

(86) Lin, H. Y.; Chen, Y. W. The Mechanism of Reduction of Cobalt by Hydrogen. *Mater. Chem. Phys.* **2004**, *85* (1), 171−175.

(87) Baumgarten, R.; Ingale, P.; Ebert, F.; Mazheika, A.; Gioria, E.; Trapp, K.; Profita, K. D.; d'Alnoncourt, R. N.; Driess, M.; Rosowski, F. Controlling the Coke Formation in Dehydrogenation of Propane by Adding Nickel to Supported Gallium Oxide. *ChemCatChem* **2024**, *16* (8), No. e202301261.

(88) Guisnet, M.; Magnoux, P. Organic Chemistry of Coke Formation. *Appl. Catal., A* **2001**, *212* (1−2), 83−96.

(89) Larsson, M.; Hultén, M.; Blekkan, E. A.; Andersson, B. The Effect of Reaction Conditions and Time on Stream on the Coke Formed during Propane Dehydrogenation. *J. Catal.* **1996**, *164*, 44−53.

(90) Wang, T.; Jiang, F.; Liu, G.; Zeng, L.; Zhao, Z. J.; Gong, J. Effects of Ga Doping on Pt/CeO2-Al2O3 Catalysts for Propane Dehydrogenation. *AIChE J.* **2016**, *62* (12), 4365−4376.

(91) Lee, M.-H.; Cheng, C.-F.; Heine, V.; Klinowski, J. Distribution of Tetrahedral and Octahedral A1 Sites in Gamma Alumina. *Chem. Phys. Lett.* **1997**, *265*, 673−676.

(92) Wang, Y.; Qiu, L.; Zhang, L.; Tang, D.-M.; Ma, R.; Ren, C.-L.; Ding, F.; Liu, C.; Cheng, H.-M. Growth Mechanism of Carbon Nanotubes from Co-W-C Alloy Catalyst Revealed by Atmospheric Environmental Transmission Electron Microscopy. *Sci. Adv.* **2022**, *8* (49), No. eabo5686.

(93) Ţucureanu, V.; Matei, A.; Avram, A. M. FTIR Spectroscopy for Carbon Family Study. *Crit. Rev. Anal. Chem.* **2016**, *46* (6), 502−520.

(94) Chu, P. K.; Li, L. Characterization of Amorphous and Nanocrystalline Carbon Films. *Mater. Chem. Phys.* **2006**, *96* (2−3), 253−277.

(95) Chang, D. W.; Lee, E. K.; Park, E. Y.; Yu, H.; Choi, H. J.; Jeon, I. Y.; Sohn, G. J.; Shin, D.; Park, N.; Oh, J. H.; Dai, L.; Baek, J. B. Nitrogen-Doped Graphene Nanoplatelets from Simple Solution Edge-Functionalization for n-Type Field-Effect Transistors. *J. Am. Chem. Soc.* **2013**, *135* (24), 8981−8988.

(96) Roy, M.; Mali, K.; Joshi, N.; Misra, D. S.; Kulshreshtha, S. K. Deposition of Hydrogenated Amorphous Carbon Films with Enhanced Sp3-C Bonding on Nanocrystalline Palladium Interlayer. *Diamond Relat. Mater.* **2007**, *16* (3), 517−525.

(97) Hita, I.; Mohamed, H. O.; Attada, Y.; Zambrano, N.; Zhang, W.; Ramírez, A.; Castaño, P. Direct Analysis at Temporal and Molecular Level of Deactivating Coke Species Formed on Zeolite Catalysts with Diverse Pore Topologies. *Catal. Sci. Technol.* **2023**, *13*, 1288−1300.

(98) Sadezky, A.; Muckenhuber, H.; Grothe, H.; Niessner, R.; Pöschl, U. Raman Microspectroscopy of Soot and Related Carbonaceous Materials: Spectral Analysis and Structural Information. *Carbon* **2005**, *43* (8), 1731−1742.

(99) Zhang, C. C.; Hartlaub, S.; Petrovic, I.; Yilmaz, B. Raman Spectroscopy Characterization of Amorphous Coke Generated in Industrial Processes. *ACS Omega* **2022**, *7* (3), 2565−2570.

(100) Ferrari, A. C.; Robertson, J. Interpretation of Raman Spectra of Disordered and Amorphous Carbon. *Phys. Rev. B* **2000**, *61* (20), No. 14095.

(101) Ferrari, A. C. Raman Spectroscopy of Graphene and Graphite: Disorder, Electron-Phonon Coupling, Doping and Nonadiabatic Effects. *Solid State Commun.* **2007**, *143* (1−2), 47−57.